JOURNAL OF GEOPHYSICAL RESEARCH, VOL. 92, NO. D6, PAGES 6579–6613, JUNE 20, 1987

Chemistry of the Global Troposphere: Fluorocarbons as Tracers of Air Motion

MICHAEL PRATHER

NASA Goddard Space Flight Center, Institute for Space Studies, New York

MICHAEL MCELROY AND STEVEN WOFSY

Center for Earth and Planetary Physics, Harvard University, Cambridge, Massachusetts

GARY RUSSELL AND DAVID RIND

NASA Goddard Space Flight Center, Institute for Space Studies, New York

Winds and convective mixing from a general circulation model of the atmosphere have been applied in a chemical tracer model (CTM) to simulate the global distribution and temporal variability of chlorofluorocarbons (CFCs). The seasonal cycle in moist convection, with maximum activity over continents in summer, leads to an annual cycle in the surface concentration of CFCs. Emissions are retained in the lowest levels of the atmosphere during winter, and surface concentrations peak near sources. In this season, CFCs from European sources are carried by low-level winds into the Arctic. During summer, vertical exchange is more efficient, and pollutants are transported more rapidly to the middle atmosphere. Consequently, concentrations of CFCs during summer are relatively low near the surface and elevated in the middle troposphere. Time series analysis of data from Adrigole, Ireland, indicates that the model accurately simulates long-range transport of air pollution. The model reproduces global distributions and trends for CFC-11 and CFC-12 observed by the ALE experiment; however, subgrid diffusion must be introduced into the model in order to reproduce the observed interhemispheric gradient. Interhemispheric exchange occurs mainly in the upper tropical troposphere, producing a profile which increases with altitude in the southern hemisphere, in agreement with observations. The distribution of CFCs is such that it is necessary to apply important corrections to observations at surface stations in order to derive global distributions.

1. INTRODUCTION

Models based on numerical solution of the equations describing conservation of mass, momentum, and energy have contributed in an essential fashion to our evolving understanding of atmospheric circulation since the early studies by *Charney et al.* [1950] and *Phillips* [1956]. Numerical general circulation models (GCMs) have been applied widely to predict weather and to study present, past, and future states of climate. Applications to chemical tracers are more recent. Pioneering work in the modeling of global atmospheric tracers was begun almost a decade ago at the Geophysical Fluid Dynamics Laboratory (GFDL) [*Mahlman and Moxim*, 1978], and the effort has expanded more recently to include, for example, groups at Goddard Institute for Space Science (GISS) [*Russell and Lerner*, 1981], Massachusetts Institute of Technology [*Golombek*, 1982; *Golombek and Prinn*, 1986], the National Center for Atmospheric Research (NCAR) [*Covey et al.*, 1985] and Los Alamos National Laboratory [*Malone et al.*, 1986], in addition to GFDL [*Mahlman et al.*, 1980; *Levy et al.*, 1982, 1985]. It is clear that three-dimensional models have an important role to play in the years ahead as we seek to unravel the complexities of atmospheric chemistry.

The chemistry of the troposphere is sensitive to a variety of processes which together determine the abundance of OH, in some respects the most important reactive species of the atmosphere. The concentration of OH depends on solar irradiance and on the abundances of O_3, CO, CH_4, H_2O, NO_x, and hydrocarbons. Concentrations of these gases may vary widely on relatively short spatial and temporal scales. This paper is the first of a series intended to provide a global model for the physical and chemical processes responsible for the distribution of tropospheric NO_x and O_3. Budgets of these chemically active trace gases involve sources and sinks in the troposphere, exchange with the stratosphere, and complex interactions with surface and subsurface environments.

We approach this task in a sequential fashion. The first step, in the present paper, is to examine the role of atmospheric motions in the dispersal of the industrial chlorofluorocarbons (CFCs): $CFCl_3$ (CFC-11) and CF_2Cl_2 (CFC-12). Modeling the distribution and variability of CFCs provides a test for three-dimensional tracer models on both global and regional scales [*Lovelock*, 1971]. Rates for emission and removal of CFCs are moderately well known. Most importantly, the distribution in the troposphere has been carefully documented over the past eight years in the Atmospheric Lifetime Experiment (ALE) [*Prinn et al.*, 1983; *Cunnold et al.*, 1986], and limited data are available back to 1970 [*Lovelock*, 1971]. The recent study by *Golombek and Prinn* [1986] was the first to examine the ALE data set with a three-dimensional model, focusing on stratospheric distributions and global lifetimes of CFCs; their model has insufficient vertical and horizontal resolution in the troposphere to simulate in detail the observed tropospheric concentrations.

The present paper examines the tropospheric distribution of

Paper number 7D0365.
0148-0227/87/007D-0365$05.00

CFCs. We use a GCM developed at the Goddard Institute for Space Studies to calculate structure and wind fields for the atmosphere and to describe the vertical exchange of air by convection [*Hansen et al.*, 1983]. The model was formulated initially for efficient simulation of climate. It was designed to allow ready investigation of the effect of spatial resolution and to study schemes for parameterization of processes operating on small scales involving the boundary layer and cumulus convection. In the present series of studies the GCM is used to provide a set of wind fields and other variables which are employed to solve three-dimensional continuity equations for selected chemical species. It is assumed that air motions are unaffected by the trace gases considered in the chemical investigation. Early versions of the GISS model have been used in a variety of studies by *Fung et al.* [1983], *Pinto et al.* [1983], and *Heimann et al.* [1986]. We shall refer to the model as a chemical tracer model (CTM).

We have made a choice here to use the most accurate, stable, and positive definite algorithm for tracer transport [*Russell and Lerner*, 1981; *Prather*, 1986]. The wind fields used in the CTM, whether from the GCM or from other sources, are assumed accurate; the advantage of the GCM lies in providing a globally self-consistent set of winds, convergences, convective fluxes, temperatures, humidities, and cloud cover. There would be little advantage in solving the linear continuity equation for tracers with the same numerical method used for nonlinear momentum equations in the GCM. We use here novel numerical techniques which provide high resolution of the tracer distribution, consistent with the dynamical fields.

We shall show that the CTM provides an excellent simulation for most of the observed features of global and regional transport of CFCs. The model reproduces observed year-to-year trends as well as seasonal and shorter period fluctuations. Long-range transport of pollutants is accurately represented. Results are in good agreement, for example, with episodic enhancements of CFCs observed at Adrigole, Ireland, and wintertime pollution of the Arctic is simulated. The results show that the CTM can play a valuable role in the interpretation of sparse ground-based data to refine global budgets. It can also provide useful guidance in the design of optimal observing strategies. For example, the model indicates that anthropogenic sources result in higher than average concentrations of pollutants in the planetary boundary layer over the northern hemisphere. The reverse situation occurs in the southern hemisphere, where transport from the northern tropics introduces elevated levels of CFCs to the upper troposphere. Thus the model highlights the importance of vertical soundings to define the distribution of CFCs. Otherwise, one may infer an interhemispheric gradient considerably larger than the tropospheric mean.

It appears that transport of trace gases between hemispheres, as resolved by the parent GCM, is too slow to account for the CFC concentrations observed in the southern hemisphere. The problem can be resolved if we assume that deep convective mixing in the vertical has associated with it mixing in the horizontal over scales not resolved by the global model. In this paper we ascribe all discrepancies in interhemispheric transport to this diffusive mixing. Introduction of a simple parameterized diffusion, effective mainly near convergence zones in the tropics, allows satisfactory modeling of interhemispheric exchange for CFCs. We show by scale analysis that diffusion of this magnitude should have little effect on the general circulation. These CFC simulations provide a quantitative evaluation of the impact of subgrid, mesoscale mixing on global tracer transport and place upper limits on its magnitude. Elsewhere, it is shown that this empirical approach also gives good agreement for the latitudinal distribution of ^{85}Kr [*Jacob et al.*, this issue]. We are continuing to assess the importance of subgrid diffusion for other chemical tracers and for the circulation itself, through direct inclusion in the GCM.

Background material on the model is given in the appendices. The parent GCM is discussed in Appendix A; the CTM, in Appendix B; and initialization procedures, release rates, and stratospheric loss for CFCs, in Appendix C. Global characteristics of the CFC simulations are discussed in section 2. Comparisons with observations at specific sites are presented in section 3. Potential applications of the CTM are described in section 4.

2. Model Results: Global Properties

The series of global CFC simulations using the CTM are summarized in Table 1 and Figures 1–13. The distributions of CFC-11 and CFC-12 were initialized in model year 1976. A uniform concentration was assumed for each hemisphere, and an initial interhemispheric difference was adopted from early measurements as described in Appendix C. Annual release rates were taken from CMA estimates, as shown in Table C1. Loss rates were based on photochemical destruction integrated over the stratospheric layers of the model for each latitude and season (see Table C4). The method of calculating advection and convection of tracers is described in Appendix B, sections B1–B5. Horizontal mixing, occurring on scales not resolved by the grid, is parameterized in the CTM by a diffusion coefficient which is proportional to the local intensity of deep convection and to the square of a length parameter D (see Appendix B, section B6). Values of D in the range 177–250 km were chosen in order to reproduce the observed CFC interhemispheric gradients; the area D^2 may be regarded as a measure of the size of a region disturbed by the largest tropical convective complexes. Winds and dynamical fields were taken from a 4° × 5° GCM. The CTM was run with both 4° × 5° and 8° × 10° resolution, as discussed later.

2.1. *Interhemispheric Transport: Effects of Resolution and Diffusion*

Detailed comparison between model runs and observed concentrations was made primarily for the period 1980–1982, using data from the Atmospheric Lifetime Experiment [*Prinn et al.*, 1983; *Cunnold et al.*, 1986] and from the Australian station at Cape Grim [*Fraser et al.*, 1985]. Results from model years 1980 and 1981, using the global 8° × 10° CTM with D = 250 km, are given in Table 1. We include also in Table 1 results from a CFC-11 calculation which used the second year of winds from the GCM for the 6-year simulation and from a CFC-12 calculation in which the parameterized diffusion was reduced by a factor of 2 (D = 177 km).

Concentrations of CFCs are significantly higher in the northern hemisphere than in the southern hemisphere, reflecting the predominance of the northern source. Air moves southward across the equator carrying a relatively high concentration of CFCs, balanced by a northward flow of air containing, on average, a lower concentration. This exchange re-

TABLE 1. CFC Annual Budget Summary

	CFC-11, 10^6 kg			CFC-12, 10^6 kg		
	1980	1981	1980*	1980	1981	1980†
Year (begin)	3618	3813	3619	5915	6272	5915
Year (end)	3813	4003	3814	6272	6648	6272
Interhemispheric difference	87	86	87	117	121	167
Interhemispheric flux						
by advection	24	23	24	38	40	56
by diffusion	94	93	94	133	138	116
Source	265	264	265	392	412	392
Stratosphere loss	−70	−71	−69	−34	−36	−34
Time Scales, year						
N-S exchange	0.74	0.74	0.74	0.68	0.68	0.97
Production	14.0	14.8	14.0	15.5	15.7	15.5
Loss	53.	53.	54.	178.	177.	178.
Relative Stratospheric Loss						
January	0.97	0.97	0.97	0.98	0.98	0.98
February	0.99	0.99	0.99	0.99	1.00	0.99
March	1.02	1.02	1.02	1.01	1.01	1.01
April	1.03	1.03	1.02	1.01	1.01	1.01
May	0.99	0.99	0.99	0.98	0.98	0.98
June	0.95	0.95	0.95	0.95	0.96	0.95
July	0.93	0.93	0.93	0.94	0.94	0.95
August	0.96	0.96	0.96	0.97	0.97	0.97
September	1.02	1.02	1.02	1.01	1.01	1.01
October	1.06	1.06	1.06	1.04	1.04	1.04
November	1.06	1.05	1.06	1.05	1.05	1.06
December	1.04	1.03	1.04	1.05	1.05	1.05
Relative Interhemispheric Flux						
January	1.85	1.88	1.45	1.64	1.62	1.67
February	1.37	1.38	1.39	1.19	1.18	1.23
March	1.30	1.30	1.09	1.23	1.23	1.28
April	0.76	0.75	0.79	0.84	0.84	0.87
May	0.77	0.76	0.84	0.96	0.97	0.99
June	0.64	0.62	0.74	0.90	0.91	0.94
July	0.55	0.52	0.61	0.80	0.81	0.83
August	0.62	0.60	0.59	0.78	0.79	0.78
September	0.71	0.70	0.59	0.76	0.76	0.70
October	1.09	1.11	1.19	1.02	1.02	0.92
November	1.27	1.29	1.03	1.07	1.08	1.02
December	1.09	1.10	1.71	0.80	0.80	0.78

*CFC-11 simulation initialized on January 1976 and run through 1980 with second year of GCM winds and convection patterns.

†CFC-12 simulation initialized on January 1976 and run through 1980 with horizontal diffusion reduced by one half (i.e., D = 177 km).

sults in a net interhemispheric transfer of CFCs. The net flux across the equator, $\Phi_{N\to S}$, may be evaluated using the CTM to integrate fluxes of CFCs. Alternatively $\Phi_{N\to S}$ may be inferred from the calculated (or observed) annual increase, given knowledge of sources and sinks within each hemisphere. The latter procedure removes the influence of seasonal migration of the tropical convergence zone, as discussed later.

A time constant for exchange between hemispheres, τ_{ex}, can be defined by

$$\tau_{ex} \equiv (M_N - M_S)/\Phi_{N\to S} \quad (1)$$

where M_N and M_S denote the total mass of tracer in the northern and southern hemispheres, respectively. In the event that emissions were suspended, the interhemispheric difference $(M_N - M_S)$ would decay exponentially with a time constant initially equal to $\frac{1}{2}\tau_{ex}$. If the hemispheres could be represented by well-mixed boxes with a barrier between, $\Phi_{N\to S}$ would be proportional to the absolute difference in mixing ratios $(M_N - M_S)$, and τ_{ex} would have a constant value independent of tracer distribution. In a three-dimensional model, however, spatial variations of mixing ratio may be quite complex, particularly in the tropics where the exchange occurs. The value of τ_{ex} in this case can vary for different species, depending on the spatial and temporal distribution of sources and sinks.

In the CFC experiments summarized in Table 1, the annual mean interhemispheric flux is approximately half the magnitude of the northern source and greatly exceeds the size of both southern sources and stratospheric losses. Values of τ_{ex} are similar for CFC-11 and CFC-12, reflecting the overall similarity of emission patterns and distributions. Two successive years of GCM winds produce nearly identical exchange times. The difference in τ_{ex} between the two CFC-12 experiments, D = 250 km versus D = 177 km, reflects a change in $M_N - M_S$; the value of $\Phi_{N\to S}$ is virtually identical for all values of D, reflecting a near steady state balance between emissions and tropospheric redistribution.

There is a large seasonal variation in $\Phi_{N\to S}$ associated with the annual migration of the convergence zone in the tropics. For example, during January and February the Hadley cell of the northern hemisphere follows the sun and crosses the equator into the southern hemisphere, bringing high levels of CFCs with it. Most of this air is not incorporated directly into the circulation of the southern hemisphere and remains in the northern branch of the Hadley circulation. This annual cycle leads to a maximum in the formally defined flux across the equator during northern winter, as shown in Table 1. The second year of GCM winds produces maximum exchange in December rather than in January. Choice of D does not change the basic seasonal pattern. The seasonal amplitude of interhemispheric mixing is much smaller than the seasonal variations in $\Phi_{N\to S}$ indicated by Table 1; the true annual cycle in interhemispheric mixing may be inferred from the modest

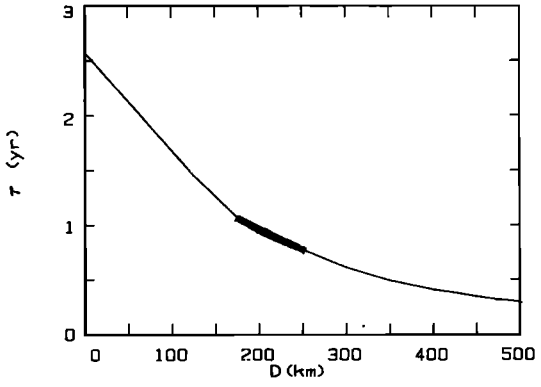

Fig. 1. Annually averaged interhemispheric exchange time τ calculated for CFC-11 as a function of the scale factor D (in kilometers). The thick part of the curve indicates the range of values which produced acceptable CFC simulations. A value of D = 250 km has nearly equivalent interhemispheric transport as uniform horizontal diffusion with coefficient 8×10^5 m^2 s^{-1}.

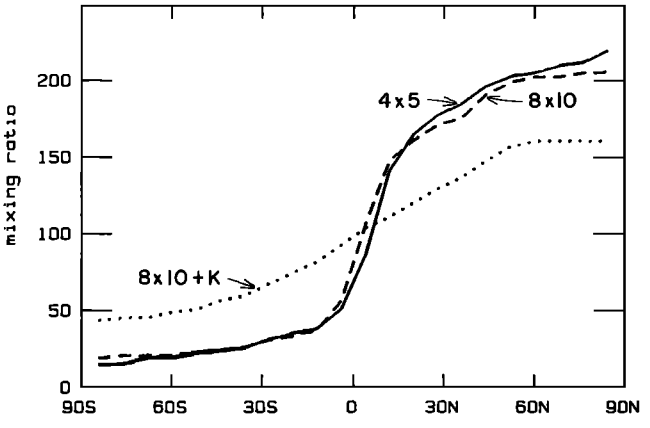

Fig. 2. Latitudinal profiles of the zonally and vertically averaged tropospheric concentrations of an artificial tracer. The simulations used a source proportional to the electric power grid, began on January 1 with no tracer, ran for 1 year, and finished with an average mixing ratio of 100 (arbitrary units). Three CTM calculations are shown: 4° × 5° with $D = 0$ (solid line); 8° × 10° with $D = 0$ (dashed line); and 8° × 10° with $D = 250$ km (dotted line). The fraction of total tracer in the southern hemisphere for these three runs at the end of December is 0.163, 0.166, and 0.344, respectively.

magnitude of seasonal variations predicted and observed for southern stations (see section 3.1).

Interhemispheric exchange of CFCs depends on the value chosen for the diffusion length D. Numerical experiments with CFCs as tracers led to an empirical relation between τ_{ex} and D, as shown in Figure 1. Values of the diffusion length as small as 100 km can have a major impact on interhemispheric transport but have little effect on the distribution of tracer outside of latitudes $\pm 20°$ (see Figure 2 and later discussion of relative transports by advection and diffusion in Figure 4). The thick part of the curve in Figure 1 denotes the range of D, 175–250 km, for which the global simulations of CFCs are acceptable, based on comparison with ALE data. The corresponding values of τ_{ex} range from 0.7 year for $D = 250$ km to 1.0 year for $D = 177$ km. As shown by *Jacob et al.* [this issue], the lower part of this range ($D = 177$–200 km) provides excellent agreement with the latitudinal distribution of ^{85}Kr observed in a series of eight Atlantic cruises [*Weiss et al.*, 1983].

The effect of grid resolution on the CTM was tested in a pair of 1-year simulations, using both 4° × 5° and 8° × 10° global CTMs, with results shown in Figure 2. The winds in both cases are based on the same run of the 4° × 5° GCM, and horizontal diffusion has been eliminated ($D = 0$). Computational costs of the global 4° × 5° CTM did not permit a multiyear simulation of CFCs, and in order to make meaningful 1-year runs, electric power consumption (described in Appendix C, section C1, and given in Table C2) was used to define a continuous source of emission for an atmosphere initially without tracer. Comparing zonal mean profiles of tropospheric concentrations at the end of 1 year, we note that the 8° × 10° CTM has a greater latitudinal domain of high concentrations, which may be thought of as defining the northern hemisphere. The demarcation of hemispheres, as defined by the steepest gradient in the tracer, occurs about 4° further

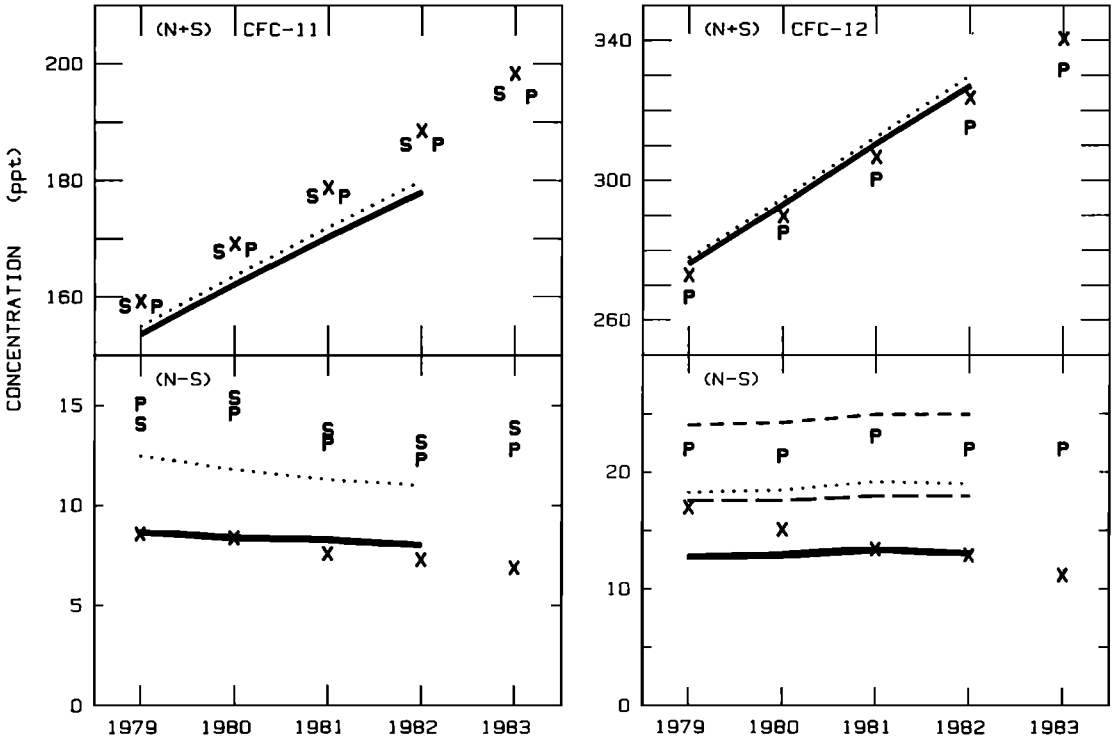

Fig. 3. Global trends in CFC-11 and CFC-12. The increase in the globally averaged concentrations of CFCs, $(N + S)$, is reported from the ALE data analysis (S for silicone column, P for Porasil column) and from GMCC data analysis (crosses). The lower panels show the trend in the interhemispheric difference $(N - S)$. All values are based on 12-month averages except for GMCC, for which the reported values are used. The model results are based on simulated data sampled at the ALE sites (dotted lines) and on true hemispheric averages (solid lines), using a diffusion scale length of $D = 250$ km. Results from the calculation of CFC-12 with reduced diffusion ($D = 177$ km) are also shown (short-dashed line for ALE sites, long-dashed line for true inventory).

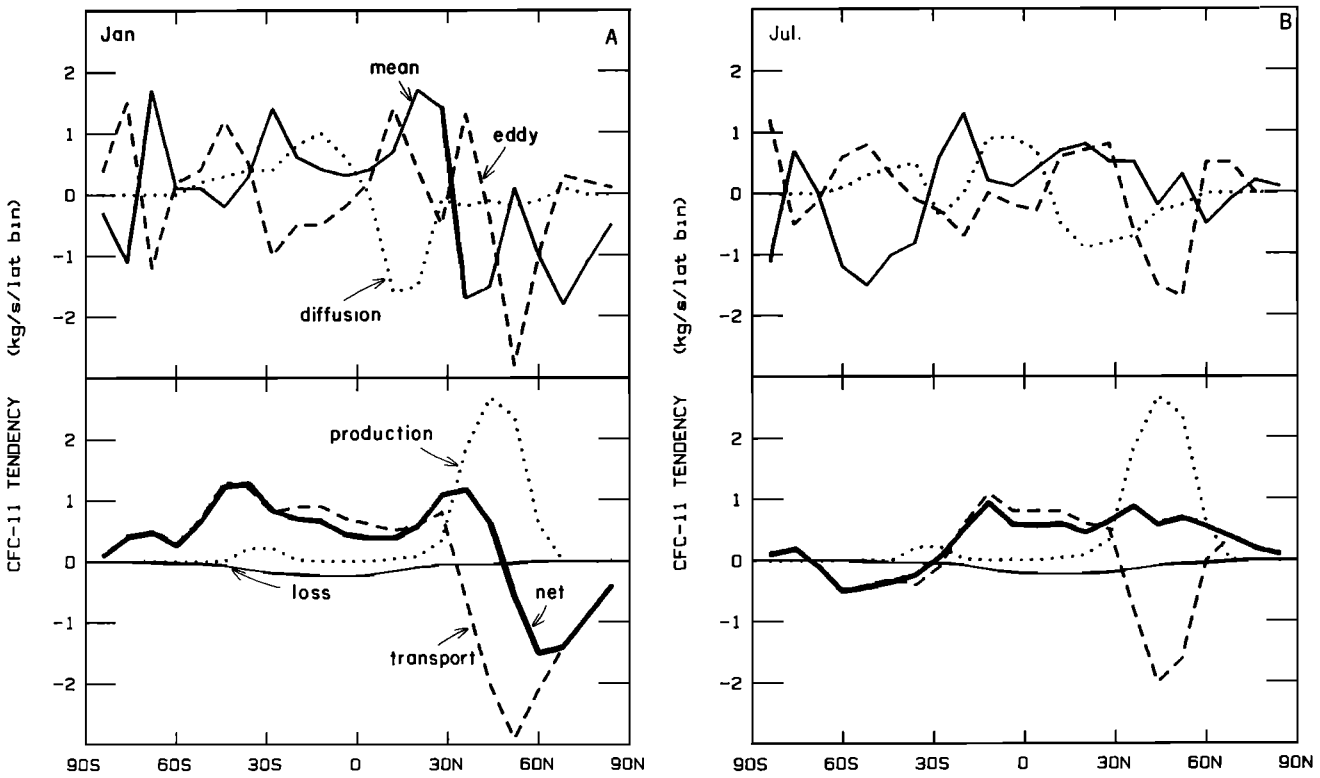

Fig. 4. Latitudinal tendency of CFC-11 for (*a*) January 1981, (*b*) July 1981, and (*c*) annual average of 1981. The units of CFC-11 tendency are kilograms per second per 8° latitude belt. The upper panels show the three components of transport due to atmospheric circulation from mean winds (solid line), resolve eddies (dashed lines) and diffusion (dotted lines). The lower panels show the net atmospheric transport (dashed lines), sources (dotted lines), stratospheric loss (thin line), and the total net change (thick line) over the period.

north in the 4° × 5° CTM, but the total content of each hemisphere has not been substantially altered. Net interhemispheric exchange is equivalent in both runs. The same CTM experiment was repeated for the 8° × 10° resolution including diffusion, with $D = 250$ km; the amount of tracer transported into the southern hemisphere doubled. These experiments demonstrate that (1) small values of D chosen for our standard models enhance the rate of interhemispheric exchange by 50–100%, and (2) increased resolution of the CTM does not substantially alter either interhemispheric transport or latitudinal distributions in the case where the same 4° × 5° wind field is used for both coarse and fine resolutions.

2.2. *Global Trends and Budgets*

The calculated trends for the global mean tropospheric concentration ($C_N + C_S$, where C_N is the concentration in the northern hemisphere, and C_S the concentration in the southern hemisphere) of CFC-11 and CFC-12 are compared with those derived from the ALE network and from the National Oceanic and Atmospheric Administration (NOAA) Geophysical Monitoring for Climatic Change (GMCC) network (crosses) in Figure 3. In Figure 3, S and P denote the silicone and Porasil columns of the ALE chromatographs, respectively [*Prinn et al.*, 1983]. The GMCC numbers have been smoothed by a curve-fitting procedure [*NOAA*, 1986]; the ALE and CTM results have been smoothed using a 12-month running average of the monthly means. Model values (designated by lines in Figure 3) show a growing underestimate of the CFC-11 global burden (by about 5% (9 ppt) as of January

Fig. 4. (continued)

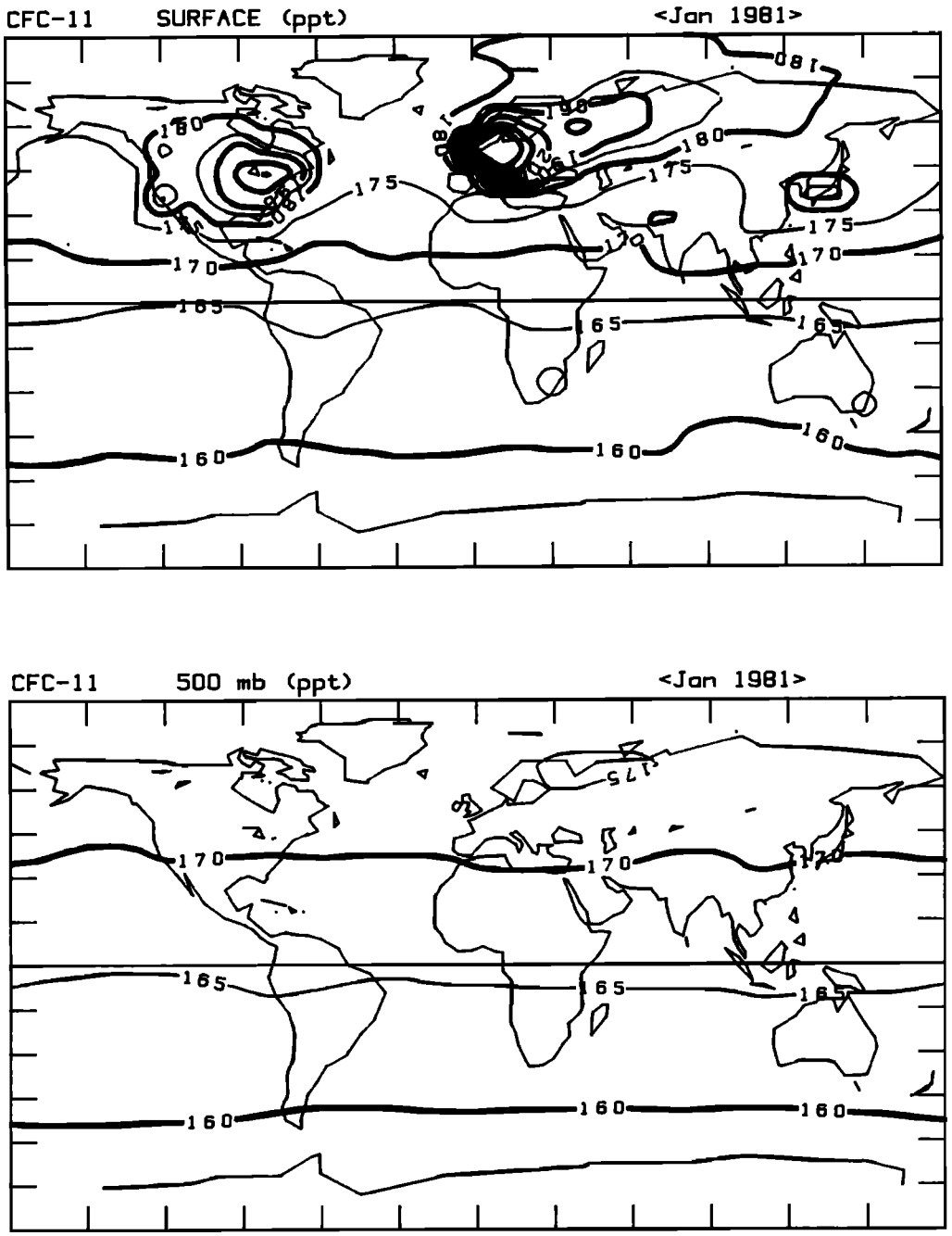

Fig. 5. Contours of CFC-11 concentrations (in parts per trillion) at the surface and at 500 mbar, averaged over the month of January 1981 from the model.

1981), when compared with the composite data from ALE and GMCC. The calculated global burden of CFC-12 is marginally greater than the ALE and GMCC values. Discrepancies of this magnitude may be explained by the acknowledged uncertainties in three critical components: (1) absolute calibration of the ALE data (see discussion of *Bullister and Weiss* [1983] by *Cunnold et al.* [1986]); (2) CMA estimates of global emissions, in particular, CFC production by the U.S.S.R. ([*U.S.S.R.*, 1986], see Table C3); and (3) the atmospheric lifetime. For example, if the instantaneous lifetime of CFC-11 was 75 years, rather than 53 years, as calculated from the simplified stratospheric loss in the CTM (see Appendix C, section C2, and Table 1), then computed CFC-22 concentrations would be greater by 7 ppt in January 1978 and by 9 ppt in January 1981.

Figure 3 also displays the trend in interhemispheric differences ($C_N - C_S$) estimated by the observational networks and by two methods of sampling using the model: from the ALE sites (dotted line, $D = 250$ km), and from the true tropospheric inventory (solid line, $D = 250$ km). The sensitivity to horizontal diffusion was examined with a 6-year simulation of CFC-12 initialized on January 1976, using $D = 177$ km (long dashes for true inventory, short dashes for ALE sites). Reducing the diffusion coefficients by a factor of 2 results in a 40% increase in the magnitude of $C_N - C_S$. The two values for D (177 km and 250 km) provide models which bracket the

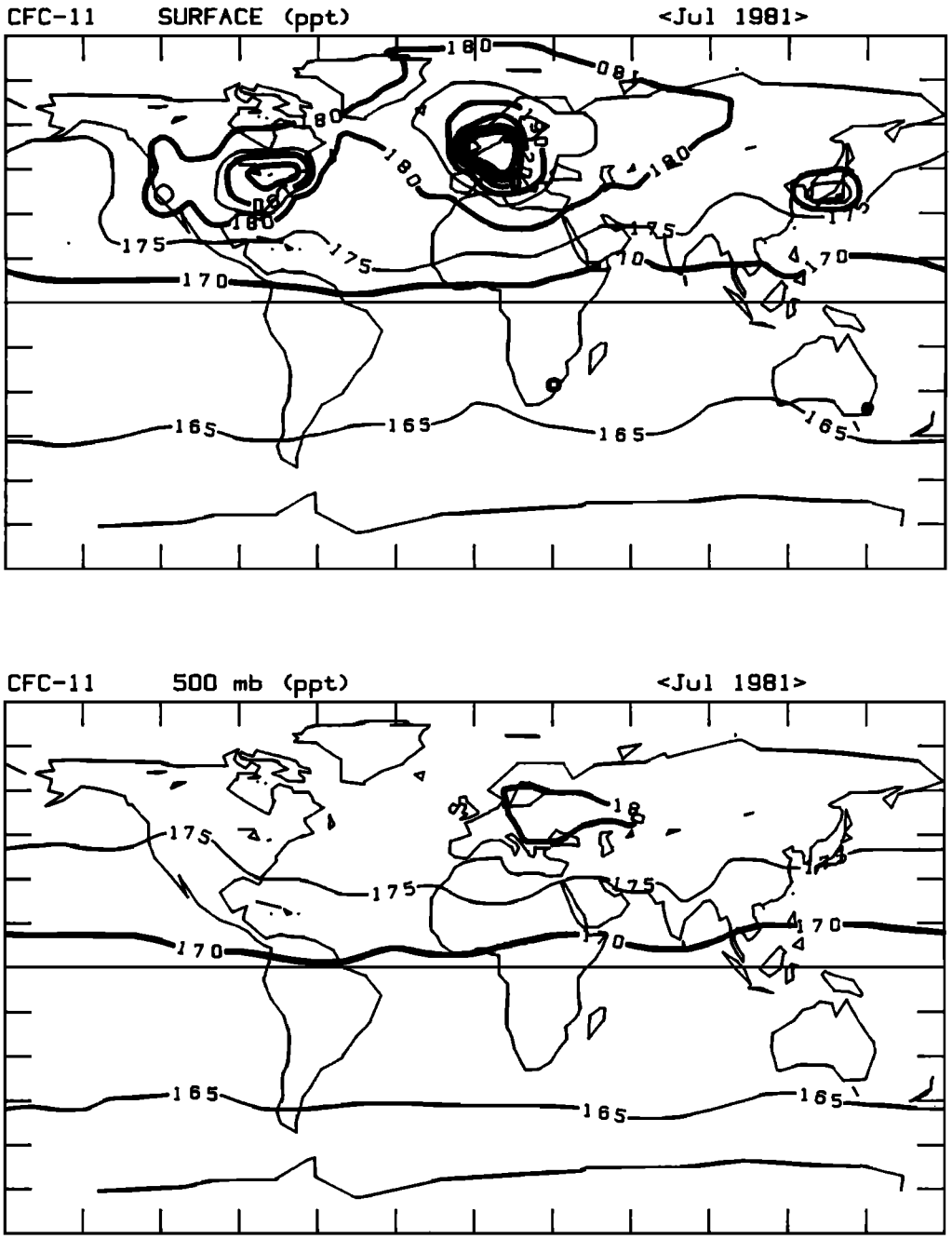

Fig. 6. Contours of CFC-11 concentrations (in parts per trillion) at the surface and at 500 mbar, averaged over the month of July 1981 from the model.

ALE data. Further refinement of the model for ALE sites requires examination of the simulated time series from higher resolution calculations, as discussed in section 3.

ALE surface stations, located relatively near continental souces (i.e., Europe, North America, Atlantic Ocean), tend to overestimate abundances of CFCs in the northern hemisphere, even when pollution events are carefully removed, as in the ALE analysis. This particular location of sites may explain partly the lower values for interhemispheric differences observed from the NOAA sites, located predominantly over the mid-Pacific (see Figure B1). Model results demonstrate that CFC data from surface sites may be systematically biased with respect to true atmospheric means, as seen in Figure 3 by comparing values derived from ALE sites with true tropospheric means. The sampling error associated with use of ALE surface sites is less than 2% for the global abundance $C_N + C_S$, but it appears to be as large as 35% for the hemispheric difference $C_N - C_S$. When pollution episodes from nearby continental sources are properly accounted for in the model, as discussed in section 3.3, the error in $C_N - C_S$ derived from ALE sites remains relatively large, about 25%.

The lack of an obvious trend in the absolute difference $C_N - C_S$ in both the ALE data and in the simulation indicates that the model is maintaining the correct balance between hemispheres by transporting approximately 45% of the northern source into the southern hemisphere. The maintenance of

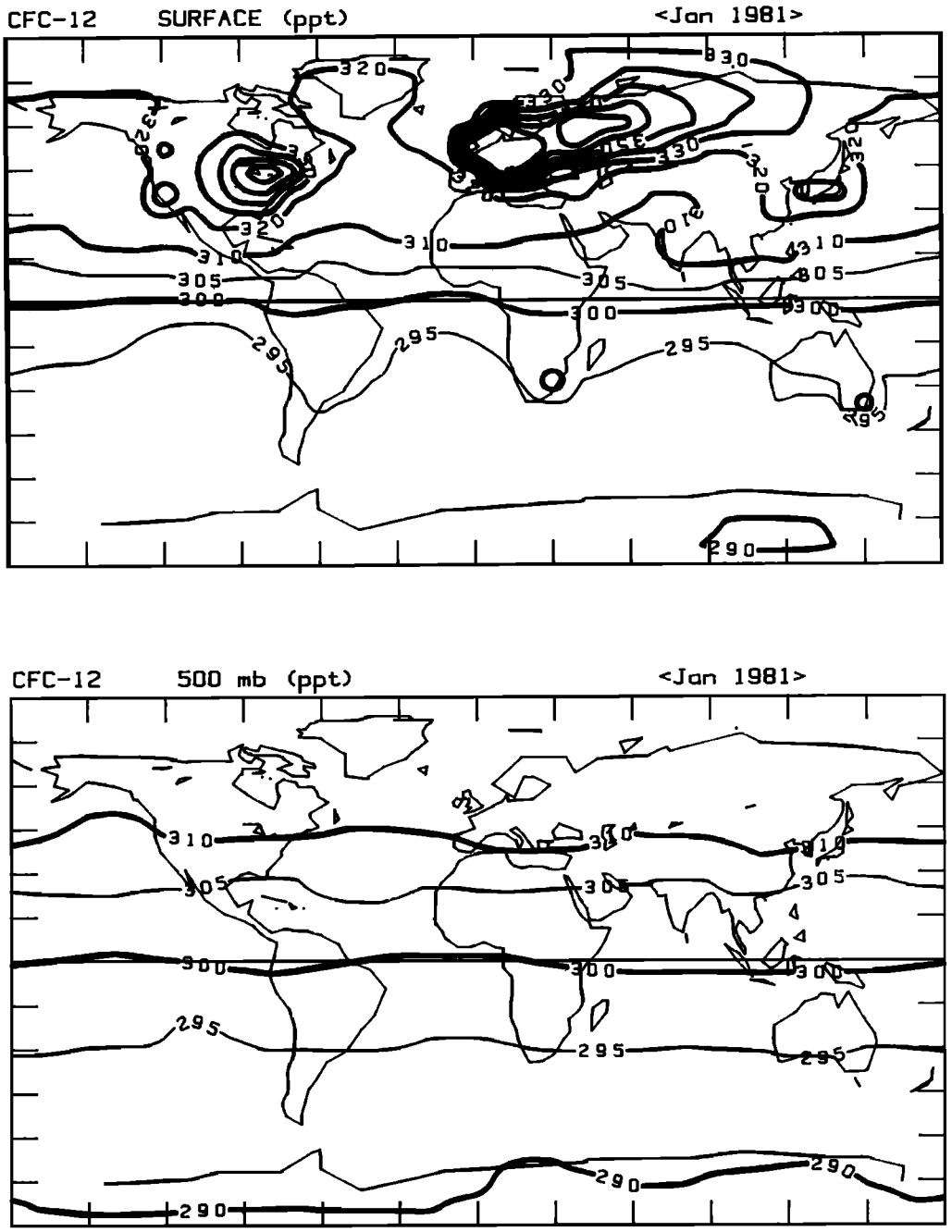

Fig. 7. Contours of CFC-12 concentrations (in parts per trillion) at the surface and at 500 mbar, averaged over the month of January 1981 from the model.

a uniform gradient, $C_N - C_S$, over the 4-year period suggests that a steady state has been reached between the release of CFCs in the north and transport to the south. Such a steady state is to be expected, since the release rate was essentially constant ($\pm 10\%$) over the period 1978–1982 (see Table C1) and since the time scale for interhemispheric mixing is about 1 year.

It is unfortunate that CFC-11 and CFC-12 are so nearly in steady state with respect to the redistribution of the gases in the troposphere, since an empirical determination of the rate of interhemispheric transport requires then an accurate measurement of the difference in concentrations between hemispheres. As we have seen, the hemispherically averaged absolute difference $C_N - C_S$ is a difficult quantity to measure, because of unavoidable sampling bias. A better method might be based on the study of a gas characterized either by an instantaneous release or by a rapid growth in emissions. In this case the rate of rise in the two hemispheres would be different, providing a more direct means for measurement of the rate of interhemispheric transport.

Figure 4 summarizes the rates of change in CFC abundance (i.e., tendency) within each latitude band due to emission, stratospheric loss, mean transport, eddy transport, and diffusion. Tendencies were defined for the months of January and July and for the annual average. The upper panels in Figures 4*a*–4*c* show the individual components of transport. Changes

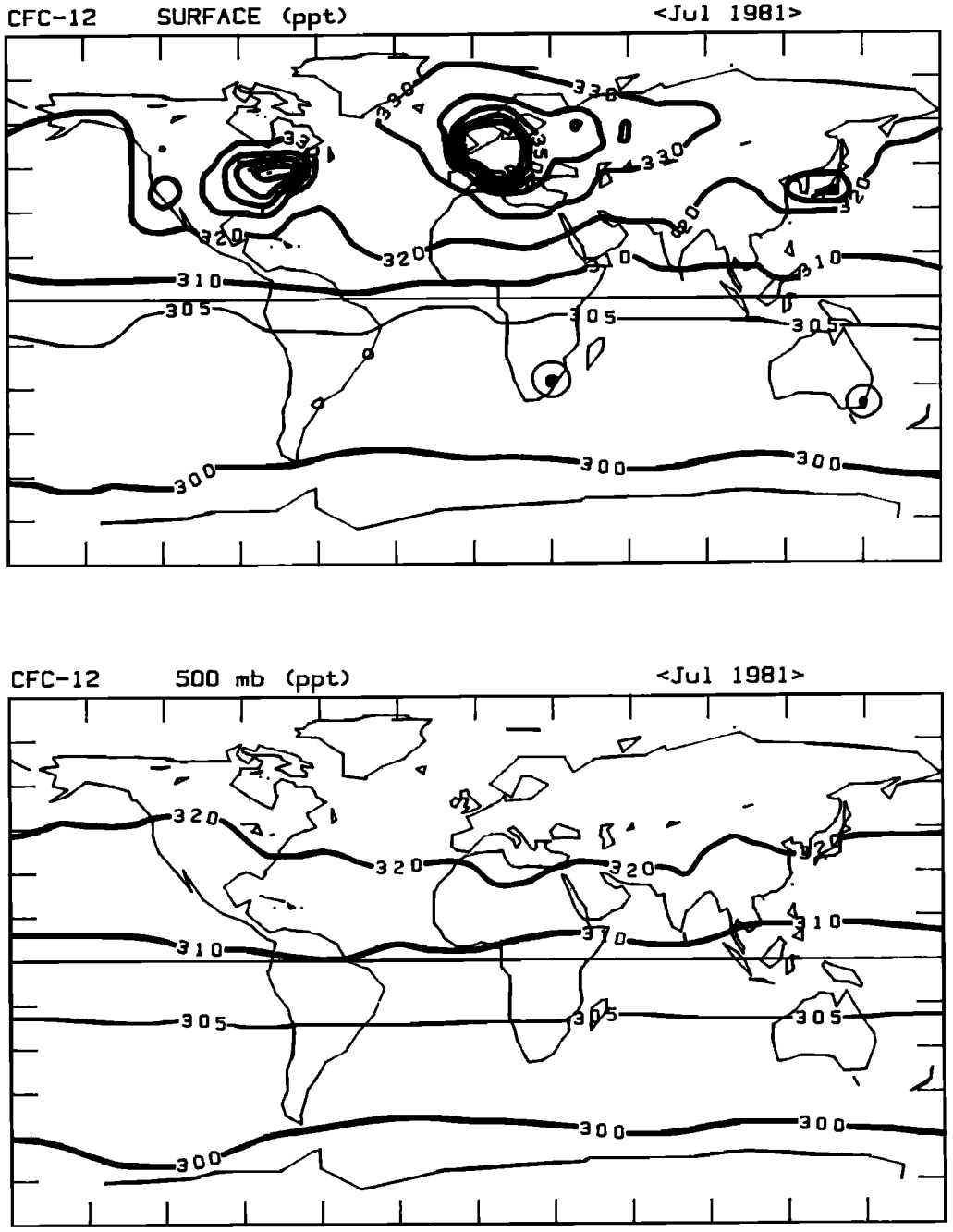

Fig. 8. Contours of CFC-12 concentrations (in parts per trillion) at the surface and at 500 mbar, averaged over the month of July 1981 from the model.

due to eddy transport (dashed line) tend to cancel those from the mean circulation (solid line); however, frictional dissipation in the form of convection and diffusion preclude a perfect balance. Transport by diffusion (dotted line) is comparable to that due to eddies plus mean circulation only in the tropics. It is dominant near the equator. The largest eddy and mean transports tend to occur in the winter mid-latitudes of both hemispheres. Similarly, the largest divergence in net total transport, attributed to southward transport by eddies, is seen in January. The lower panels in Figures 4*a*–4*c* show that stratospheric loss (thin line) is negligible and that emissions (dotted line) are balanced over the year by mean atmospheric transports (dashed line). The annual net tendency (thick line in lower panel of Figure 4*c*) produces a uniform rate of increase per unit area over the globe. The redistribution of CFC sources is variable for individual months, and net transport on short time scales may occur in a sense counter to the mean latitudinal gradient.

Stratospheric losses and lifetimes are summarized in Table 1. Losses show only a small semiannual cycle. Calculated lifetimes are subject to an uncertainty of $\pm 30\%$, since the structure of CFC-11 and -12 in the stratosphere is not resolved with the nine-layer CTM. The instantaneous lifetime of 53 years for CFC-11 corresponds to a steady state lifetime of the order of 45 years, within the lower ranges calculated by two-dimensional photochemical models [*Ko and Sze*, 1982; *Owens*

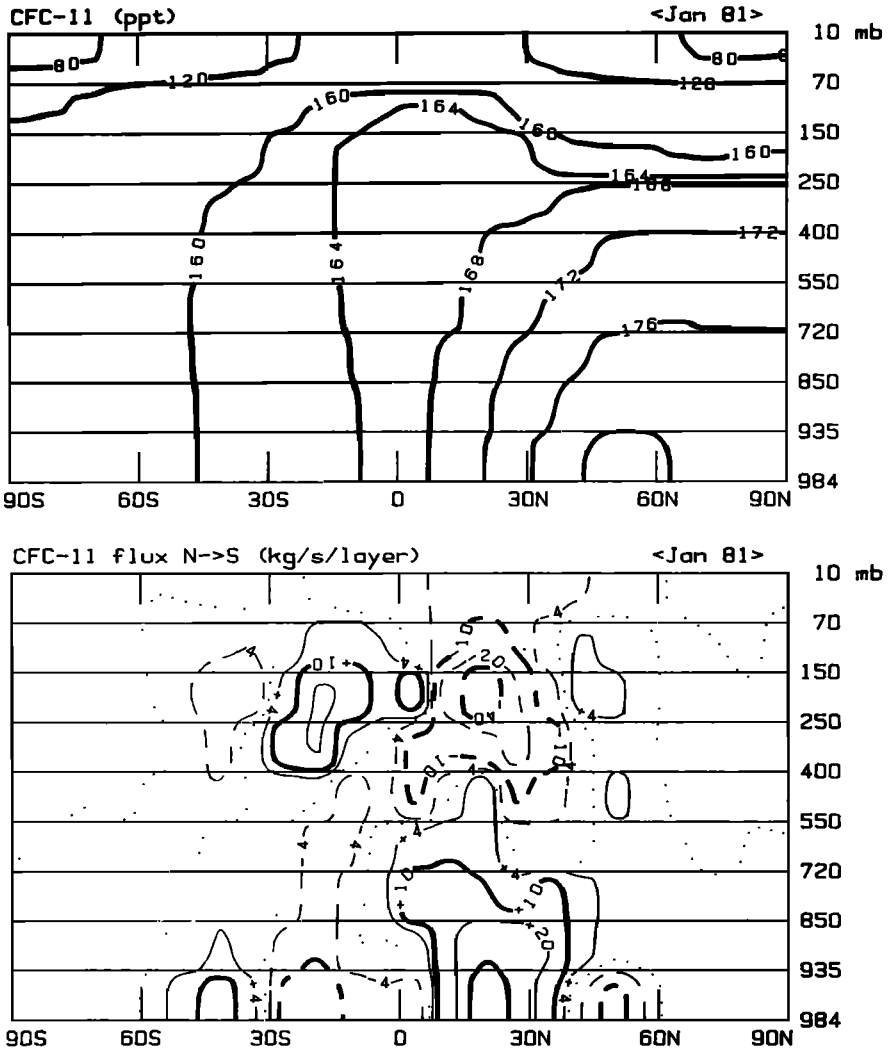

Fig. 9a.

Fig. 9. Altitude-by-latitude contours of CFC-11 concentrations (in parts per trillion) and total southward flux of CFC-11 (in kilograms per second per layer) for (*a*) January, (*b*) April, (*c*) July, and (*d*) October of 1981. The data are contoured by σ-layer; the pressure coordinates shown for the edges of the layers correspond to a surface pressure of 984 mbar. Positive, southward fluxes are given by solid contours; negative fluxes are denoted by dashed contours; and the zero line, by a dotted line. Contour intervals for the fluxes are ± 4(thin), ± 10(thick), ± 20(thin), and ± 40(thick) kg s^{-1} layer^{-1}.

et al., 1982; *Jackman and Guthrie*, 1985]. A lifetime of 75 years would lead to better agreement with the observed global burden of CFC-11, as discussed previously. Our derived instantaneous lifetime for CFC-12 of 178 years is greater than the two-dimensional steady state calculations, which give a range of 120–140 years; concentrations computed here would be reduced by about 1–2% if the two-dimensional results were adopted. Stratospheric losses are unaffected by different choices of winds and diffusion, as shown in Table 1.

The oceans represent a potential sink, or at least a reservoir, for CFCs released into the atmosphere. Observations indicate that CFCs are present to considerable depths in the ocean [*Gammon et al.*, 1982]. The solubilities of CFC-11 and CFC-12 in seawater have values about 67–71% of those for fresh water [*Wisegarver and Cline*, 1985; *Warner and Weiss*, 1985]. The dimensionless solubility coefficient K_H (i.e., moles of CFC dissolved in a liter of water divided by the moles of CFC per liter of air) ranges from 0.57 at 0°C to 0.13 at 30°C for CFC-11 in seawater. The corresponding values of K_H for the less soluble CFC-12 are 0.15 and 0.04, respectively. To obtain a first-order estimate of the oceanic content of CFC-11, we could use observations of the mixed layer depth of CFCs (120–140 m; *Gammon et al.* [1982]) and a mean value of K_H to calculate a fractional abundance, ocean/atmosphere, of 0.3%. A more detailed model gives 0.5–1% for CFC-11 in the sea, with a factor of 3 less for CFC-12 (R. Gammon, private communication, 1986). Oceanic contributions to current CFC budgets are consequently negligible. For long time scales, if the entire ocean approaches equilibrium with the atmosphere, as much as 14% of the total CFC-11 would reside in the ocean.

2.3. *Spatial Distribution of CFCs*

Monthly averaged concentrations of CFC-11 and CFC-12 are shown for the surface and 500 mbar in Figures 5–8. Steep longitudinal gradients, associated with continental sources, are

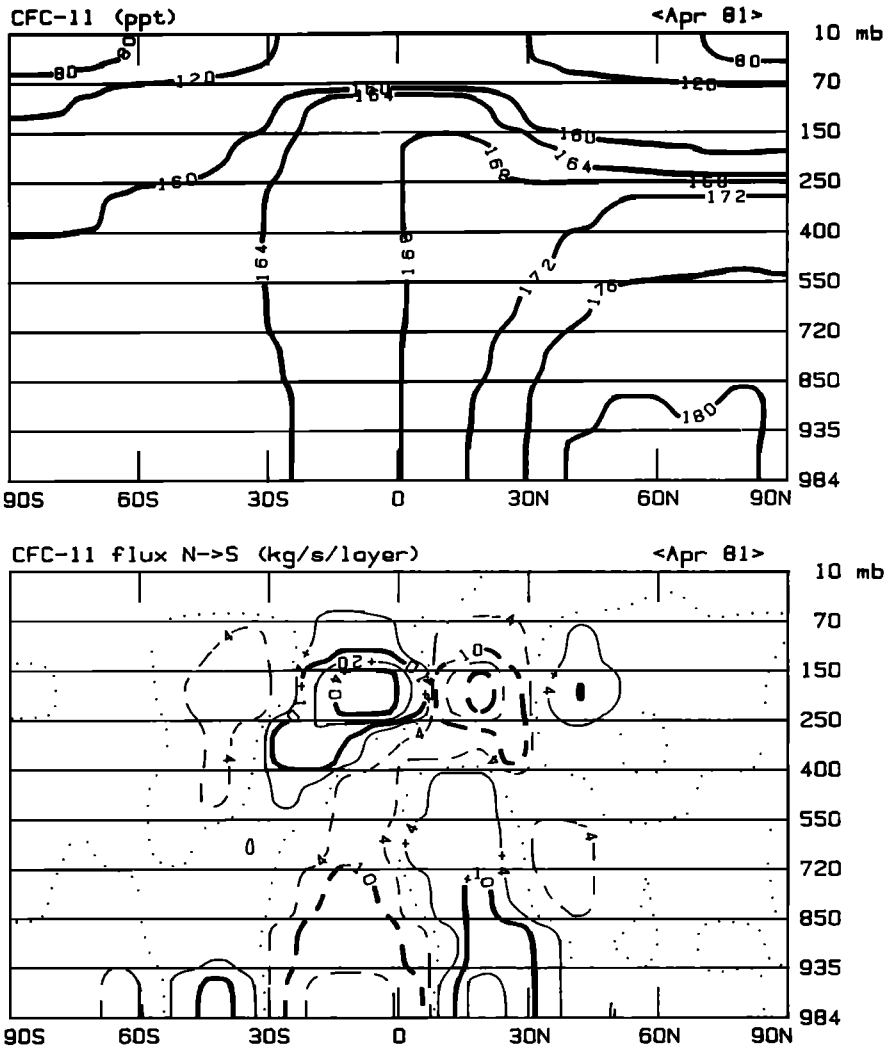

Fig. 9*b*.

predicted near the surface. Some structure, attributed to convective activity over the continents, is observed at 500 mbar in summer. The 500-mbar contours in winter are more zonally symmetric, however, and show little indication of sources below. Convective activity is most prevalent over continents in summer and over oceans in winter (see Figure B2). Vertical gradients in CFCs are thus largest over land in winter, when CFC emissions are most effectively contained in the lowest layers of the atmosphere. This confinement accounts also for the extensive plume of CFC-rich surface air extending northeast from Europe into the Arctic during January, as illustrated in Figures 5 and 7. Other pollutants are expected to be transported along with CFCs from the same source regions, contributing to the Arctic haze phenomenon, discussed further later.

Gradients of CFC mixing ratio across the equator are steeper at the surface than at 500 mbar, and gradients are sharper over oceans than over continents. This pattern, seen in Figures 5–8, reflects the general Hadley-type circulation, in which the mean flow converges in the tropics in the lower levels of the atmosphere and returns to each hemisphere in the upper troposphere after some exchange between hemispheres. The model calculates greater latitudinal mixing over the equatorial continents, primarily as a result of enhanced horizontal diffusion associated with much greater convective activity over land.

Vertical motions are sufficiently strong in the region of tropical convergence to ensure that CFC mixing ratios are approximately uniform from the surface to the upper troposphere. To the north of this convergence zone, concentrations decline with altitude, reflecting inputs from sources. To the south they increase with altitude, reflecting interhemispheric exchange. In January 1981 the CFC convergence zone was calculated to be near the equator at the 165-ppt contour for CFC-11. In the following July, average concentrations increased about 5 ppt, and the convergence zone is seen to occur at about 15°N, near the 170-ppt contour. The zone of tracer convergence mimics the seasonal movement of the Intertropical Convergence Zone, following the sun, as discussed in section 2.1. It usually remains in the northern tropics.

Seasonal cycles in tracer concentrations may be generated both from the annual migration of the convergence zone and from seasonal variations in transport within a hemisphere when the sources and sinks are not uniformly distributed throughout the atmosphere [e.g., *Levy et al.*, 1982]. We have shown that such seasonality depends on geographic location

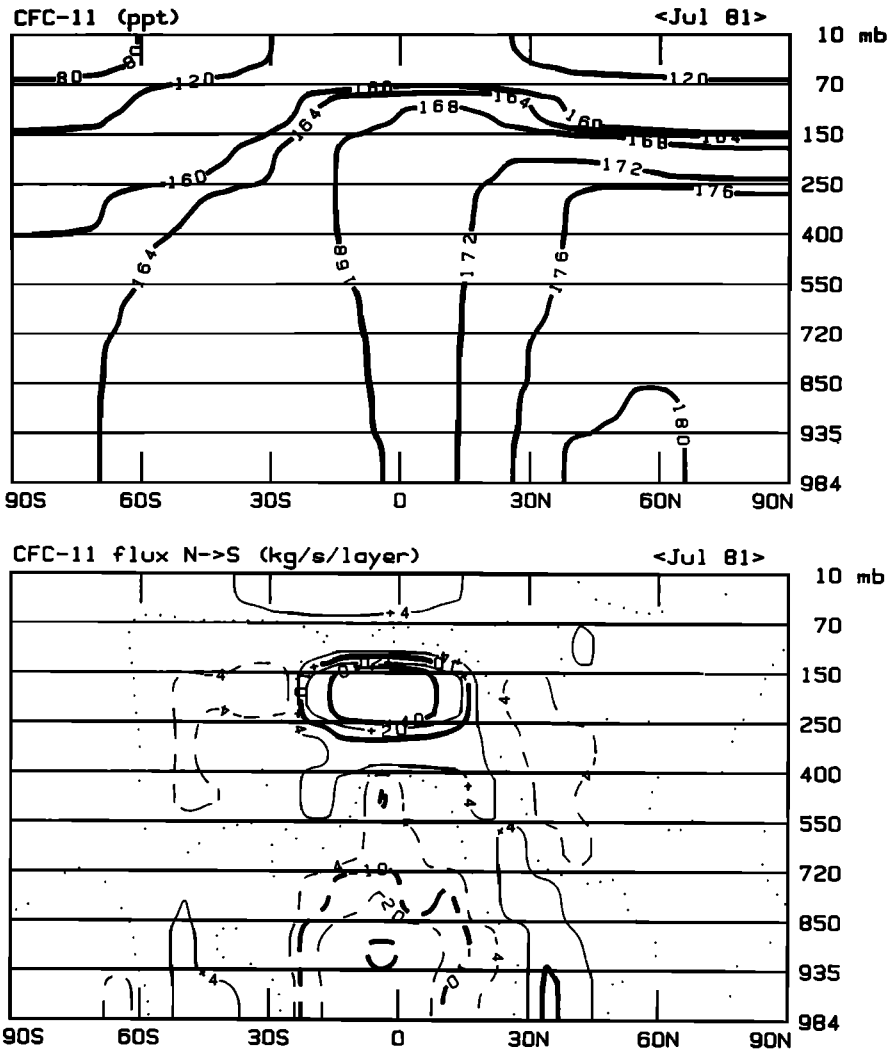

Fig. 9c.

and occurs even for chemically passive tracers with uniform rates of surface emissions (see Figures 5–8 and the analysis of station data in section 3).

Meridional cross sections of zonally averaged mixing ratios of CFC-11 are shown for 4 months of 1981 in Figure 9. In the northern hemisphere the CFC profiles decline with height as expected, as a result of the influence of surface sources. Almost all surface measurements in the northern hemisphere, no matter how clean the air being sampled, may be expected to reflect this pattern. In the southern hemisphere, concentrations increase with altitude over much of the troposphere.

The zonal average of meridional flux of CFC-11, calculated for 4 months of 1981, is shown in Figure 9 and displays the pronounced Hadley circulation in the tropics. The major southward transport from 30°N to the equator takes place in the lowest three layers, below 720 mbar. The greatest flux in the southern tropics occurs in the upper troposphere, between 100 and 400 mbar. Figure 9 displays the almost universal feature of interhemispheric transport by which air containing high levels of a tracer with a predominantly northern source, such as CFCs or CO, enters the southern hemisphere via the upper troposphere [*Newell et al.*, 1974].

3. Model Results: Detailed Comparison With Observations

3.1. *Seasonality and Trends in Station Data*

Variations in monthly mean concentrations of CFC-11 predicted by the model for 1980 and 1981 are shown for selected sites in Figure 10. Variations in the northern hemisphere generally reflect changes in the transport of CFCs from industrial source regions. Data from Point Barrow, Alaska [*Khalil and Rasmussen*, 1983] provide a useful example. This site is influenced during winter by long-range transport of CFCs and other pollutants from European source regions, as noted in Figures 5 and 7. Point Barrow is relatively isolated from source regions during summer. With the secular trend removed, the CTM predicts mean wintertime concentrations of CFC-11 which are 4 ppt greater than summetime values (Figure 10*a*). *Khalil and Rasmussen* [1983] reported wintertime enhancements averaging about 4.5 ppt for CFC-11 and 6 ppt for CFC-12, in excellent agreement with model results.

Figure 10*b* exhibits zonal asymmetries in monthly mean surface concentrations for CFC-11 around a latitude circle at

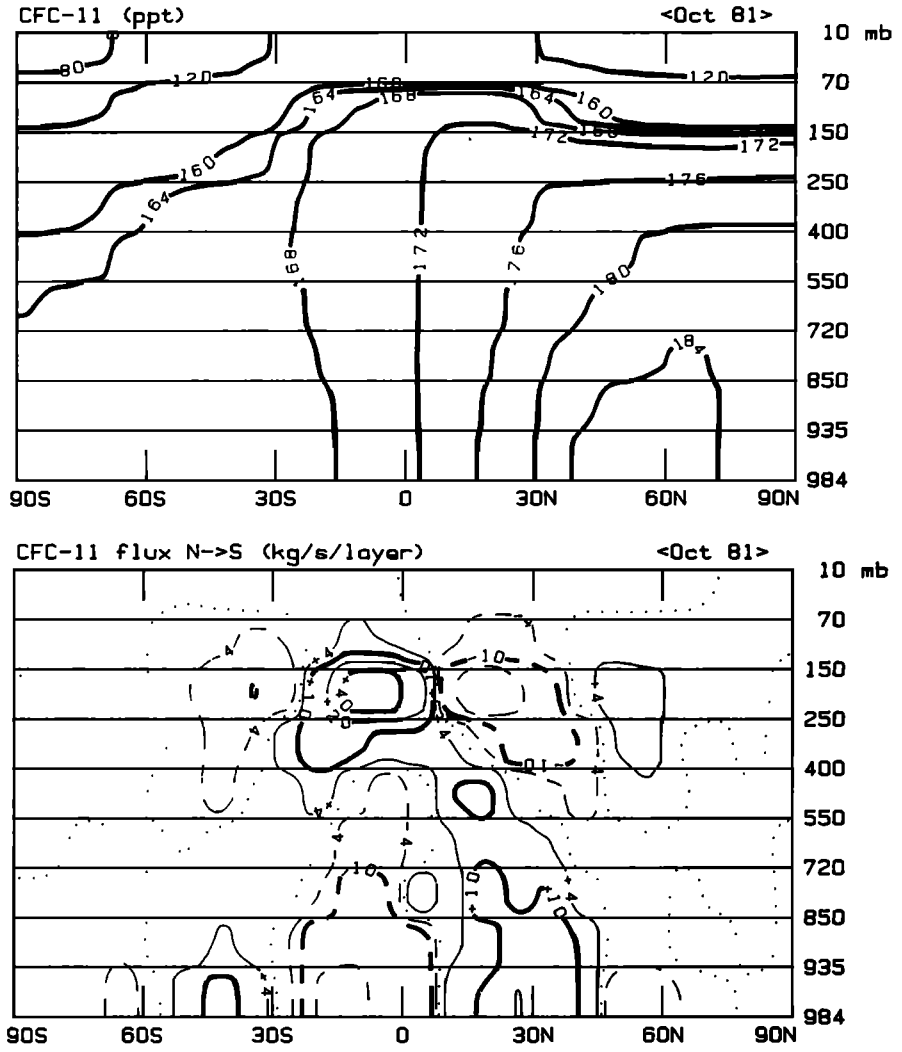

Fig. 9*d*.

44°N. The mid-Pacific values (thick solid line) are lowest and show distinct seasonal variations, with minimum values in summer. Concentrations in the mid-Atlantic Ocean (thin solid line) are consistently higher than in the mid-Pacific and have a reversed seasonal cycle (summer maximum) reflecting greater advection of CFC-rich surface air from Europe in summer. Concentrations predicted for Cape Meares, Orgeon (dotted line), and for the longitude of Ireland (dash-dot line) are typically 2–5 ppt above values at midocean sites to their west. Variations in rates of transport through the boundary layer lead to a characteristic, seasonal behavior of CFCs over continental source regions, as illustrated for the central United States (thick dashed line) and central Europe (dash-dashed line) in Figure 10. The concentration in the boundary layer is relatively high in winter and drops with the onset of convective mixing in spring. Unfortunately, few observations are available to test predictions of the magnitude of enhanced CFC concentrations in the boundary layer over source regions. Several measurements reported for Melbourne [*Fraser et al.*, 1983] show elevations of more than 100 ppt above background for CFC-11, but these data are insufficient to define a seasonal pattern. The modeled concentrations for the Adrigole site (52°N) are similar to those labeled Ireland (dash-dot line) at 44°N in Figure 10. These monthly means are sometimes greater, sometimes less than the values at Oregon (dotted line), but they average about 3 ppt higher, in agreement with the extended ALE data [*Cunnold et al.*, 1986].

The predicted differences between concentrations at the surface and those in the middle troposphere are illustrated for CFC-11 in Figure 10*c*. We have selected two locations, one where observational data exist (southern Australia) and the other where there is potential to obtain such information (Hawaii). For both locations, seasonal variations at the surface (solid line) are much larger than at 500 mbar (dotted line). The vertical differences, $C_{500\text{mbar}} - C_{\text{surf}}$, are as large as -4 ppt over Hawaii and average $+1$ ppt over Australia. The calculation is in agreement with observations over southern Australia [*Rasmussen et al.*, 1982] which show an increase in CFC-11 of about $+1$ ppt aloft.

Trends in CFC-11 and CFC-12 at the ALE sites obtained with the 8° × 10° CTM ($D = 250$ km) are presented in Figures 11 and 12 (solid line). Monthly mean model values are compared with observations of background clean air from the five ALE stations. The trend (in absolute units, in parts per trillion per year) is similar at all stations because the emissions and tropospheric redistribution of CFCs are nearly in steady state

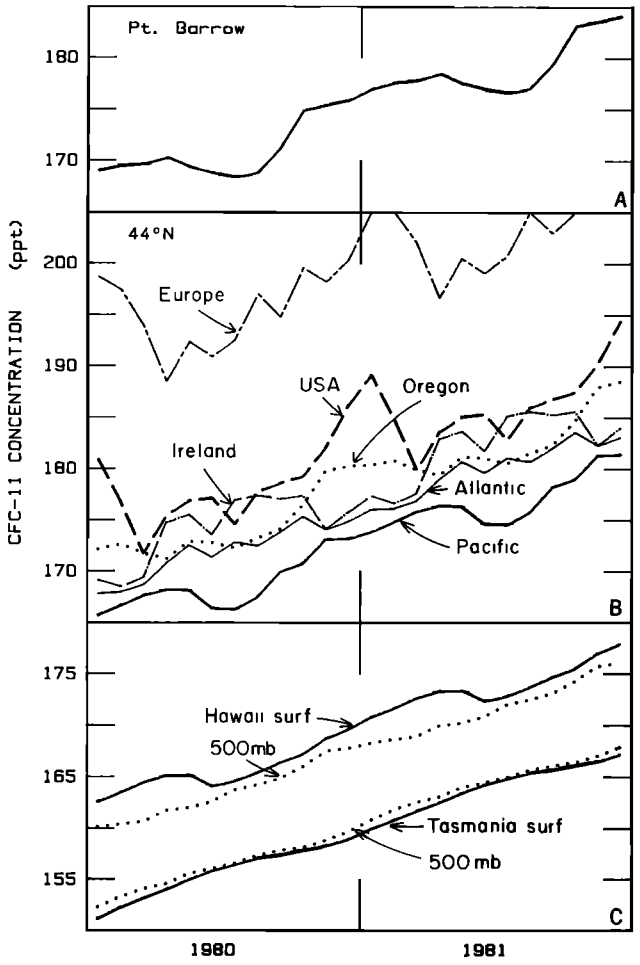

Fig. 10. Monthly mean concentrations for the years 1980–1981 from the model (*a*) at Point Barrow, Alaska, (*b*) around a latitude circle at 44°N, and (*c*) over Hawaii and southern Australia. The Point Barrow and 44°N values are all surface mixing ratios. The 44°N locations are mid-Pacific (160°W; thick solid line); Cape Meares, Oregon (dotted line); central United States (100°W; thick dashed line); mid-Altantic (20°W; thin solid line); near Ireland (10°W; thin dash-dot line); and central Europe (20°E; thin dash-dashed line). The Hawaiian (upper pair) and Australian (lower pair) sites include values for both surface (solid line) and 500 mbar (dotted line).

for the years 1978–1981. As noted in section 2.2., calculated concentrations of CFC-11 are lower than observed values by about 5%. This difference is greatest in the northern hemisphere (11 ppt) and least in the southern hemisphere (7 ppt). Computed values for CFC-12 match the ALE data within ±2% at all sites.

We recognize two problems which may occur when comparing simulations using average concentrations from the CTM with observations at a particular ALE site: horizontal gradients may not be well resolved with the 8° × 10° grid; and the ALE data have had pollution episodes removed by an algorithm involving simultaneous measurement of short-lived pollutants, a process which cannot easily be simulated in the present model runs. An important question is how well the model predicts monthly mean background concentrations (i.e., typical clear air) observed at sites adjacent to sources. These issues, horizontal resolution and pollution episodes, are examined in sections 3.2–3.3, using the high-resolution 4° × 5° CTM which is applied to the European window (and which cannot be used for lengthy global simulations). We show that for Ireland, and possibly for Oregon, background air simulating the "unpolluted" data reported by ALE lies 4–6 ppt below the average value at the site. Thus a best comparison with the reported ALE data would be made with values which lie between the mean concentrations calculated from the 8° × 10° grid box at the site and those from the less polluted grid box immediately to the west (dashed lines in Figures 11 and 12). Large spatial gradients occur also in the vicinity of Barbados for which we show the grid box immediately to the northwest (dashed line). Agreement between calculated and observed means would be excellent in this case for all stations if the total atmospheric burden were corrected to reflect a 75-year lifetime for CFC-11.

A calculation for CFC-12 with reduced horizontal diffusion (D = 177 km, dashed line) is compared with the reference model (D = 250 km, solid line) in Figure 13. As expected, differences between northern and southern sites increase by about 8 ppt when diffusion coefficients are reduced by a factor of 2. The reference model with D = 250 km overestimates interhemispheric transport of CFCs, while that with D = 177 km leads to an underestimate. The other notable change occurs at the tropical sites, which exhibit increased seasonality with reduced levels of diffusion. An optimal fit to all the ALE station data would result from values of D in the lower part of this range, 180–200 km, if we apply the arguments above and use the adjacent less-polluted grid squares to the west of Cape Meares and Adrigole (dashed lines in Figures 11 and 12) as the best simulation of background air. This value for D gives an excellent fit also to the data for ^{85}Kr [*Jacob et al.*, this issue].

The seasonal cycle in CFC-11 at southern mid-latitudes (40°S) is predicted to have a peak-to-peak amplitude of about 1 ppt (D = 250 km), which is not readily seen on the scale of Figure 11. The minimum occurs about February and the maximum near August. The phase of the variation is consistent with observations from Cape Grim, Tasmania, but the observed peak-to-peak amplitudes are greater, about 2 ppt [*Fraser et al.*, 1985]. The ALE data from Samoa have opposite phase, with relative maxima in CFCs every January–February and peak-to-peak amplitudes in excess of 2 ppt for CFC-11 [*Cunnold et al.*, 1986]. This period corresponds to the southernmost extent of the tropical convergence zones and is the most likely time for Samoa to observe northern hemispheric air with higher concentrations of CFCs. Modeled values at Samoa have nearly the same phase as the data, reaching a maximum during February–March, but have smaller amplitudes, of the order of 1.4 ppt. Calculations with reduced diffusion (D = 177 km) have increased seasonal amplitudes for CFC-12 in the southern hemisphere by about 50% and are in closer agreement with the data.

Observations of CFCs at Oregon exhibit a large, possibly seasonal, variation, but unfortunately the data record for this site is brief. Minimum concentrations were observed in summer when winds were predominantly from the west, carrying low concentrations of anthropogenic gases. Concentrations of CFC-11 and CFC-12 are predicted to be especially low over the Pacific Ocean in summer when the prevailing winds are weaker, minimizing the transport of Eurasian sources over the mid-latitude Pacific and maximizing the exchange of air with the northern tropics. During winter,

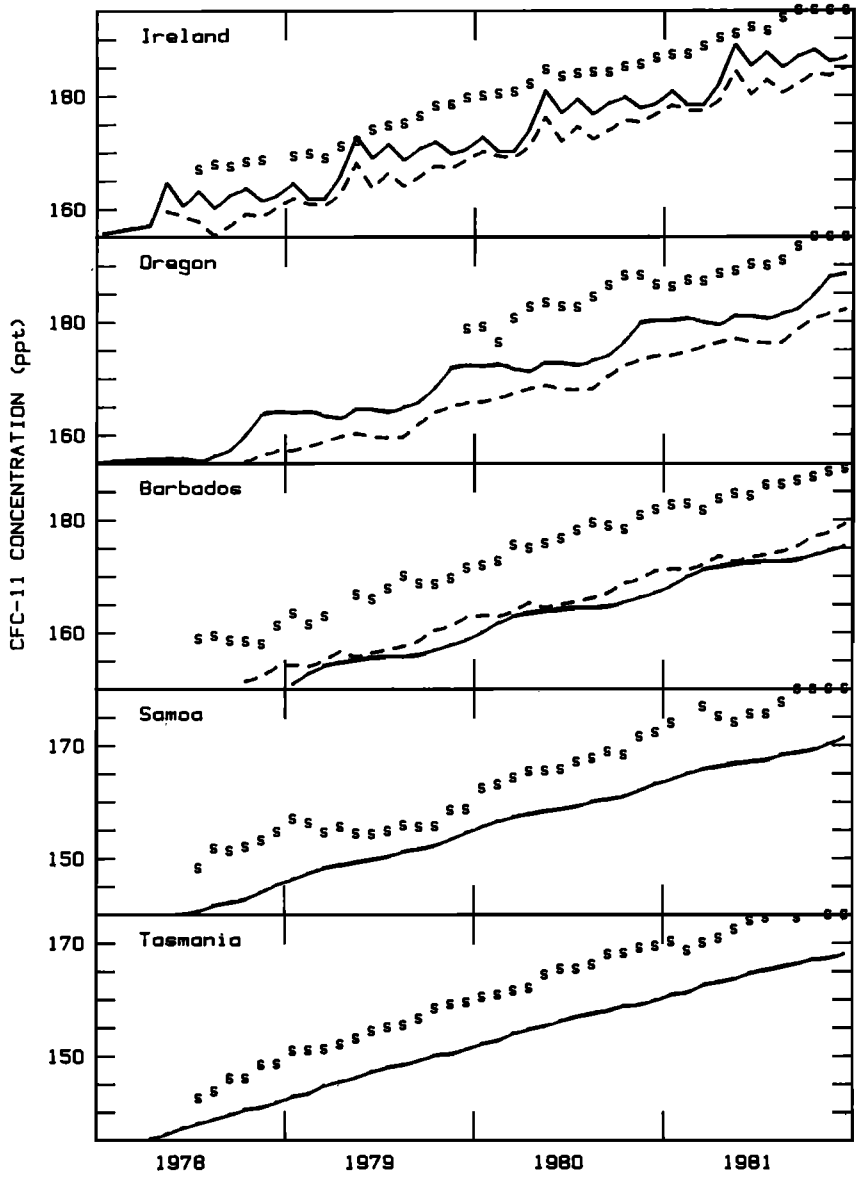

Fig. 11. Monthly mean surface concentrations of CFC-11 at the ALE sites. The reported ALE values are designated by their chromatographic column (*S*), and the calculated concentrations from the CTM are connected by a solid line. Simulated concentrations for the grid box immediately to the west of Adrigole, Ireland, to the west of Cape Meares, Oregon, and to the northwest of Barbados are shown by dashed lines in the respective panels.

background air from the Pacific shows relatively elevated levels, since the mid-latitude Pacific air is more representative of the higher concentrations at northern mid-latitudes. This effect is clearly indicated in Figures 10–13, for example, by the summer minimum in the mid-Pacific station at 44°N. Modeled concentrations of CFC-11 and CFC-12 at Oregon are influenced by winds from the south and east during fall and winter and are correspondingly higher, showing more frequent pollution episodes under these conditions. A similar pattern would be expected at the Oregon site for other gases of anthropogenic origin and could be responsible for at least a portion of the seasonal cycle reported for CO [*Khalil and Rasmussen*, 1984].

3.2. *Window Calculations for Europe*

Studies of long-range transport and dispersal of air pollution on a continental scale require a CTM with the finest possible resolution. In this case the global calculation may prove to be too expensive computationally and, furthermore, unnecessary. We have implemented a subset of the global CTM simulation in which the calculation is performed only within a window on the globe. In this section we demonstrate that window calculations of CFCs for Europe are indeed a valid subset of the global model and examine the impact of improved resolution and numerics on the simulations.

The European window covers one-sixteenth of the globe, as shown in Figure 14*a*. Winds are computed with the global

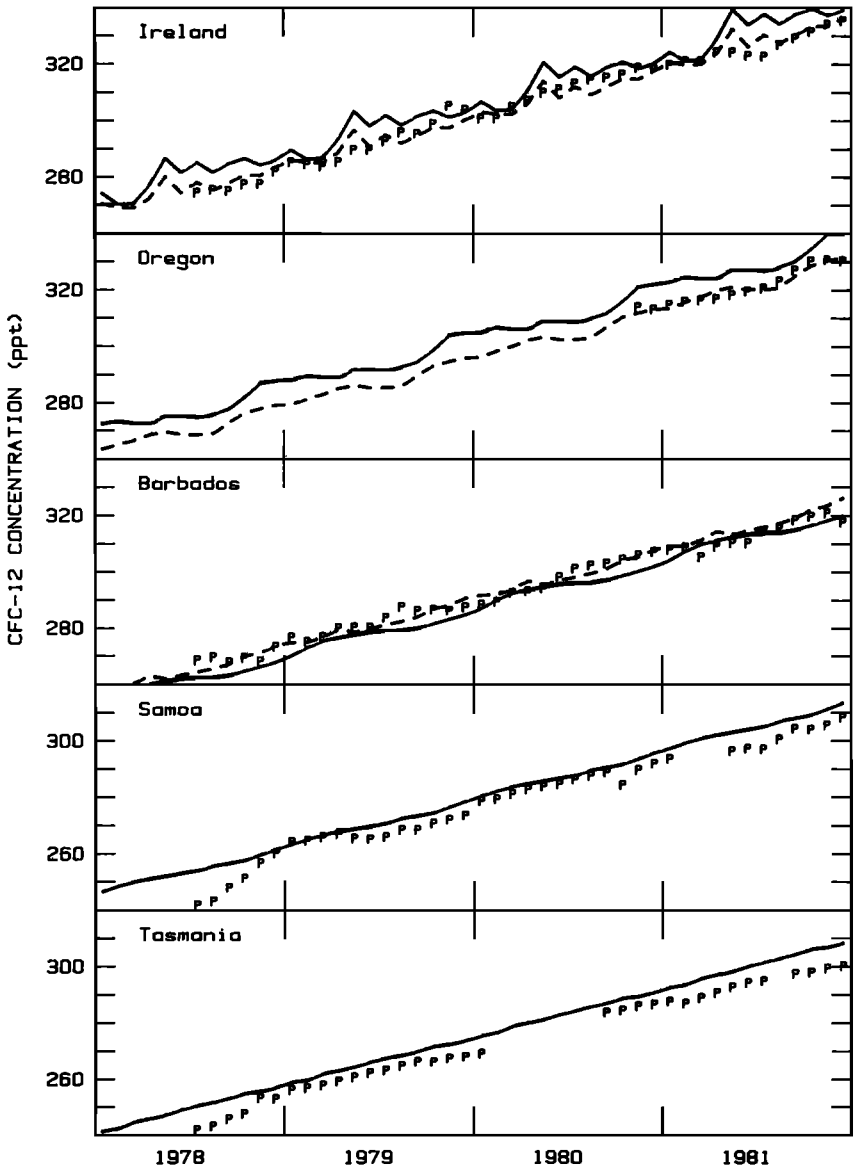

Fig. 12. Monthly mean surface concentrations of CFC-12 at the ALE sites. The reported ALE values are designated by their chromatographic column (*P*). See Figure 14.

GCM (4° × 5° resolution) and applied in the CTM, using both 4° × 5°. and 8° × 10° grids. Window calculations employed both the standard slopes advection scheme used in all global simulations as well as the more accurate second-order moments (SOM) method [*Prather*, 1986], which offers greater resolution and accuracy for both transport and emissions. Mixing ratios of CFCs were initialized throughout the volume to a concentration of 100 ppt, as were the boundary values along edges of the window. Reduced stratospheric concentrations were included, as described earlier.

High-resolution models require correspondingly fine source grids. We constructed a high-resolution 4° × 5° emission grid for CFC-11 over the European window. Countries were resolved in a 1° × 1° grid; electric power consumption for each country [*Central Intelligence Agency* (*CIA*), 1984] was distributed equally by area; scale factors relating CFC-11 emission to electric power were 1.0 for Western Europe and 0.2 for Eastern Europe, Africa and Asia; total emissions were 120 × 10^6 kg yr^{-1}, equivalent to the amount released within the European window during year 1981 of the global simulation. The second-order moments of the sources within each 4° × 5° grid were calculated by aggregating the 1° × 1° elements according to (B17). We used three source grids in these window calculations: (1) the 8° × 10° global grid, as defined in Table C2 and used in all global calculations; (2) the 4° × 5° window grid as defined above with uniform emission in each grid square; and (3) the 4° × 5° window grid, with 1° × 1° emission elements resolved by their second-order moments in each grid square.

Concentrations of CFC-11 over Europe for July 1981 from the global 8° × 10° simulation (Figure 6) are shown in Figure 14*b*, where the contours indicate values in excess of the back-

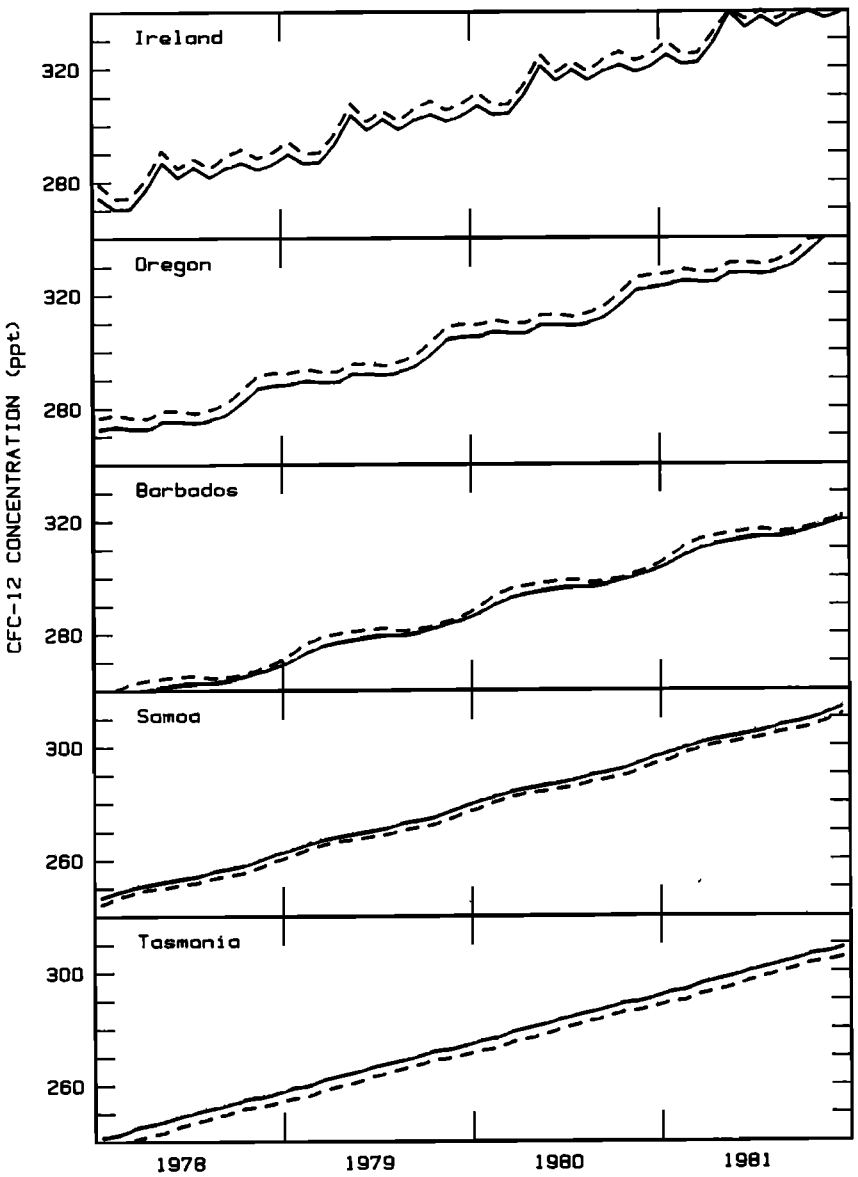

Fig. 13. Monthly mean surface concentrations of CFC-12 at the ALE sites. Simulated values are shown for the standard calculation (D = 250 km, solid line, as in Figure 15), and for the calculation with reduced diffusion (D = 177 km, dashed line).

ground level of 177 ppt. Figure 14*c* shows a comparable calculation with the 8° × 10° window on Europe, using the same source grid as the global model (source grid 1). Figures 14*b* and 14*c* are essentially identical, illustrating in this case that the window calculation provides an accurate simulation of the global results (i.e., regional sources dominate variations of surface level concentrations in the domain of the window).

Figure 14*d* shows results for January from the 4° × 5° window calculation, using SOM and the source grid 1. The finer spatial resolution and SOM algorithm keep the high concentrations of CFC-11 more contained in the vicinity of continental sources. Our best simulation is illustrated in Figures 14*e* and 14*f*, which show results for July and January from the 4° × 5° SOM simulation, using 4° × 5° sources with moments (grid 3). The winter-to-summer differences are apparent, showing the same patterns as in the global calculation, Figures 5–8. Significant improvements, as compared with the global simulation in Figure 14*b*, are due to the finer resolution of the model, including better resolution of sources.

One use of the results in Figures 14*c*–14*e* would be to correct the systematic bias of the Adrigole grid box in the 8° × 10° CTM for its proximity to the European sources. The monthly mean values at Adrigole in the 8° × 10° calculation (Figure 14*c*) range from 2 to 6 ppt higher than in the 4° × 5° SOM calculation with the same 8° × 10° source grid (Figure 14*d*). When 4° × 5° SOM sources are used (grid 3), however, the mean concentrations increase by a comparable amount because of the proximity to sources in the United Kingdom.

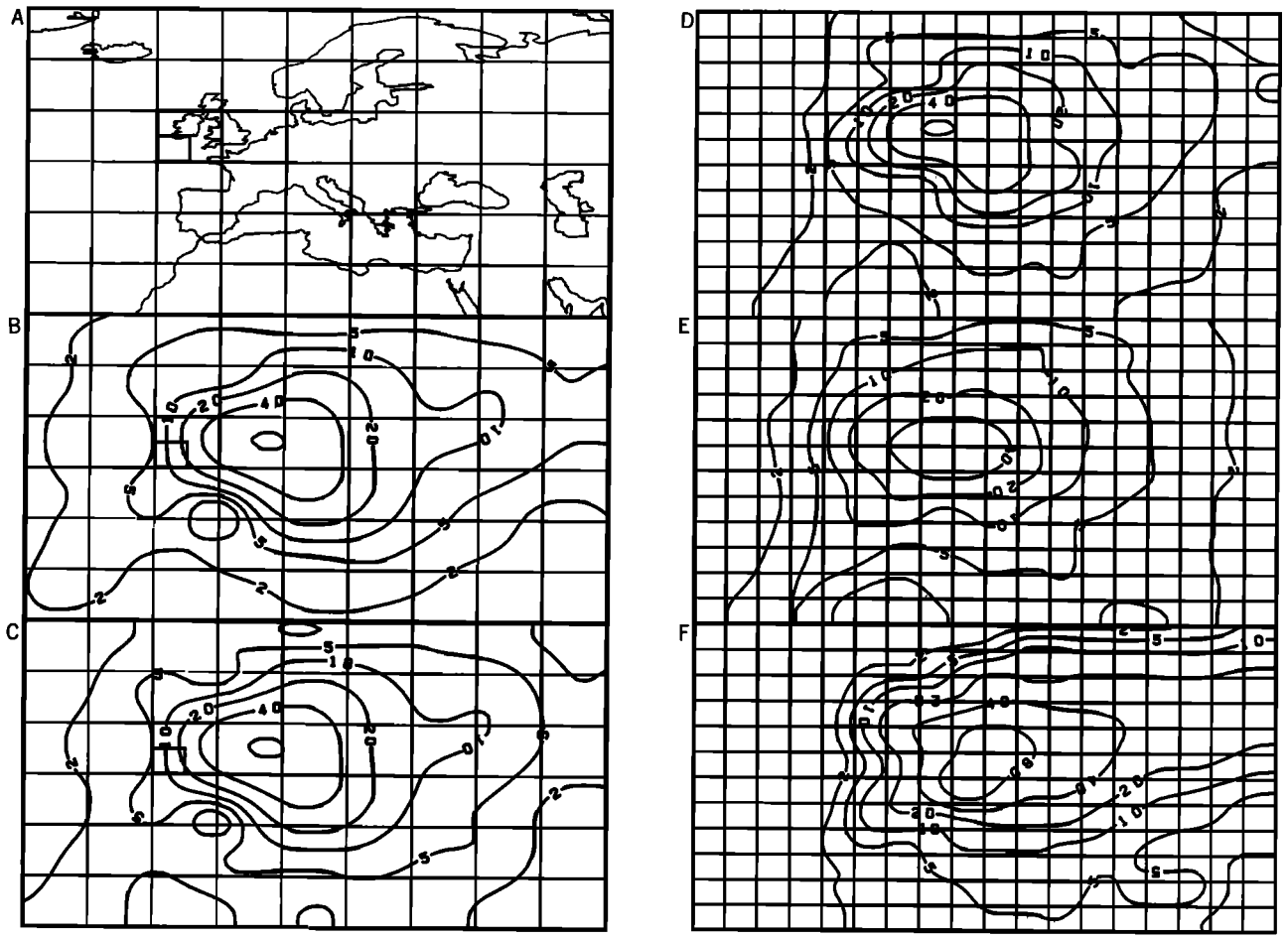

Fig. 14. Surface concentrations of CFC-11 over Europe. (*a*) Map for the European window calculation, with emboldened grid boxes identifying the location of Adrigole for both 4° × 5° and 8° × 10° grids. (*b*) Surface concentrations of CFC-11 from the global 8° × 10° calculation for July 1981; contours (in parts per trillion) have had a background level of 177 ppt subtracted in order to compare with the window calculations. (*c*) Surface values for July from the 8° × 10° window calculation; contours are in units of parts per trillion above the background level of 100 ppt. (*d*) Surface values for July from the 4° × 5° window, using second-order moments and 8° × 10° sources. (*e*) Results for July and (*f*) results for January from the 4° × 5° CTM, using second-order moments for transport and for CFC sources on a 4° × 5° grid.

Thus improved resolution of transport and sources produces little net change in the mean concentrations at Adrigole as compared with the global 8° × 10° CTM.

3.3. *Synoptic Variability and Pollution Episodes*

An important feature of three-dimensional chemical tracer models is their ability to predict the magnitude and frequency of variations in tracer concentrations at an observing site. CFC-11 has long been identified with pollution episodes in the United Kingdom [*Lovelock*, 1971; *Pack et al.*, 1977; *Penkett et al.*, 1979; *Brice et al.*, 1982]. The individual ALE measurements of CFC-11 (*S*) at Adrigole, Ireland, are plotted in Figure 15 and show numerous events during which air with high levels of CFCs was sampled at the Adrigole site. There are typically 15 major pollution episodes per year with an amplitude approximately 50 ppt or more above the (slowly increasing) background of CFC-11.

Simulations of surface concentrations of CFC-11 at the Adrigole site, obtained using both the 8° × 10° global model (sampled every 8 hours) and the high-resolution window models (sampled every 4 hours), are displayed in Figure 16. Figure 16*a* shows the time series from the finest-resolution model, the 4° × 5° CTM, using SOM and 4° × 5° sources with moments (grid 3), described previously. Figure 16*b* shows the same simulation, using the slopes method for advection and uniform emission over 4° × 5° (grid 2), and Figure 16*c* gives results from the same 4° × 5° model with 8° × 10° sources from Table C2. Figure 16*d* shows the time series from the 8° × 10° CTM model with source grid 1. The magnitude and frequency of pollution episodes in the best model (Figure 16*a*) look remarkably like the ALE time series in Figure 15. The effect of coarser resolution is seen in the sequence from Figure 16*a* to 16*d* and appears as a flattening of the episodes, leading to lower peak intensities and longer durations.

One method of defining the background, unpolluted con-

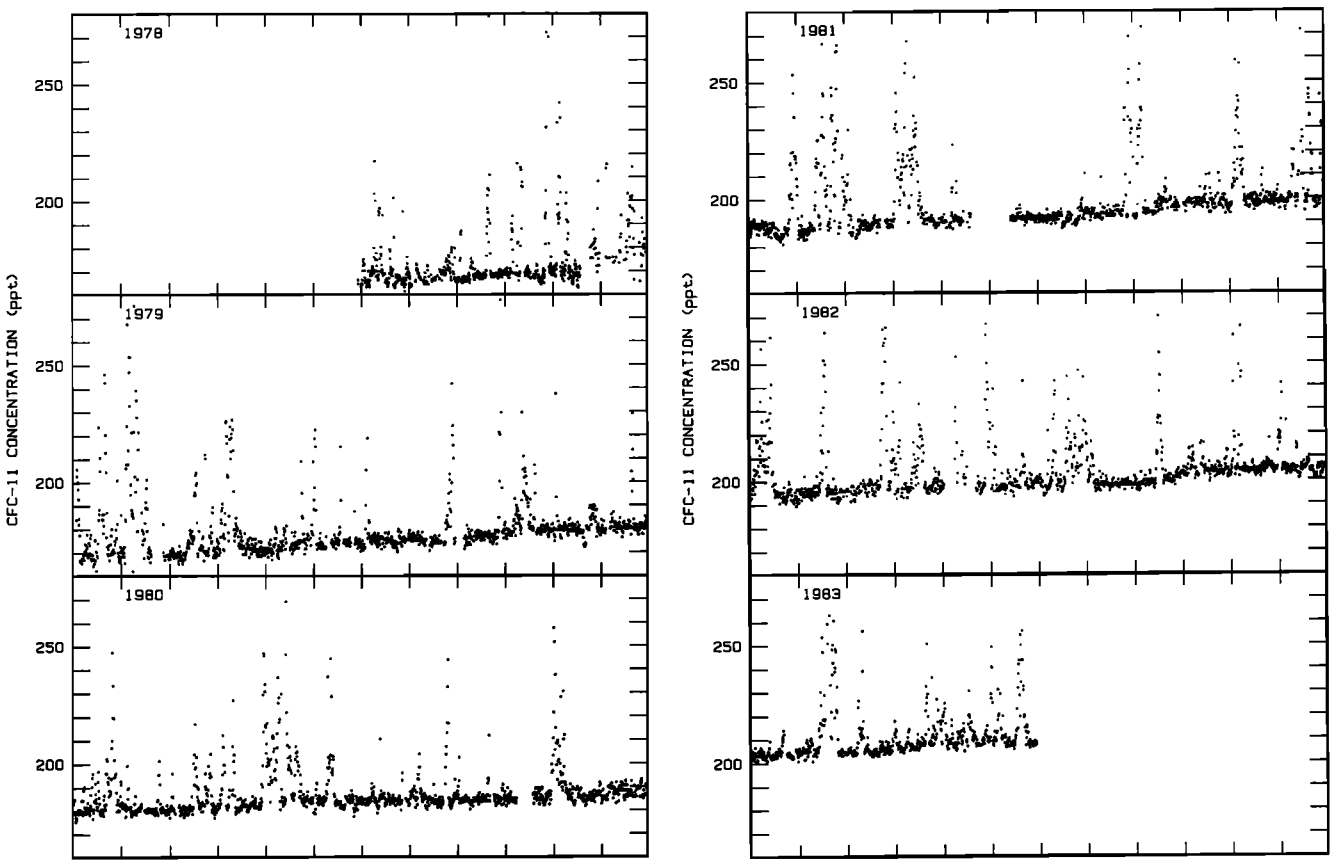

Fig. 15. Time series of individual observations of CFC-11 (S) reported by ALE at Adrigole, Ireland.

centration of CFCs at Adrigole is based on the probability distribution of observed concentrations. We remove a linear fit from the ALE data shown in Figure 15 and plot the sorted residuals on a probability scale, as shown by the solid line in Figure 17. The lowest 70% of ALE observations fall on a straight line, which corresponds to a normal distribution with variance (3 ppt)^2; the upper 30% of the data comprise pollution events and raise the total variance to (11 ppt)^2. A measure of the background atmosphere is given by the median value (fiftieth percentile), which is approximately 5 ppt below the mean value. Probability distributions of the 4° × 5° SOM simulation (short-dashed line) and the 8° × 10° slopes simulation (long-dashed line) are also shown in Figure 17. The distribution of modeled concentrations for the 4° × 5° grid to the east of Adrigole is included in Figure 17 (dotted line) as an example of a more polluted region; this grid contains significant emissions associated with the United Kingdom and would measure background air less than 20% of the time. The 8° × 10° model fails to describe the upper 20% of the pollution events. The 4° × 5° model adequately reproduces the Adrigole environment, for which the background concentration (median) is on average 4–5 ppt below the average.

Pollution events simulated by the CTM do not coincide specifically with the observed episodes at Adrigole, since the model is meant to reproduce a typical year rather than a particular one. One method of examining and comparing the climatology of pollution episodes is by calculating the autocovariance $AC(f, \Delta)$ of the tracer concentration over a time interval T,

$$AC(f, \Delta) = \frac{1}{T}\int_0^T [f(t+\Delta) - \bar{f}][f(t) - \bar{f}]\, dt \qquad (2)$$

where $f(t)$ denotes the mixing ratio at time t, Δ denotes the lag, and the average value of f is $\bar{f}$, which may also include a linear trend where appropriate. The value $AC(f, 0)$ is equal to the variance (ppt^2) in the time series. The normalized autocorrelation function, defined as $AC(f, \Delta)/AC(f, 0)$, describes the probability that elevated concentrations will be observed at times Δ before or after the peak event.

Autocovariances of the ALE data for CFC-11 (S) at Adrigole have been presented by *Prather* [1985], and similar calculations for the 5-year record [*Cunnold et al.*, 1986] are reproduced in Figure 18. Pollution events are seen to have an average variance of 125 ppt^2 above the background, a half-height half-width duration of 2 days, and an extended shoulder with consistently elevated concentrations out to 8 days. The extended shoulder reflects the large spatial extent of the CFC emission region in Europe.

Autocovariances for three CTM simulations of the Adrigole time series are also given in Figure 18. In this comparison with observations we have tried to remain consistent with recent estimates for European emissions [*European Council of Chemical Manufacturer's Federations* (*CEFIC*), 1985] and have rescaled the source of CFC-11 within the CTM window

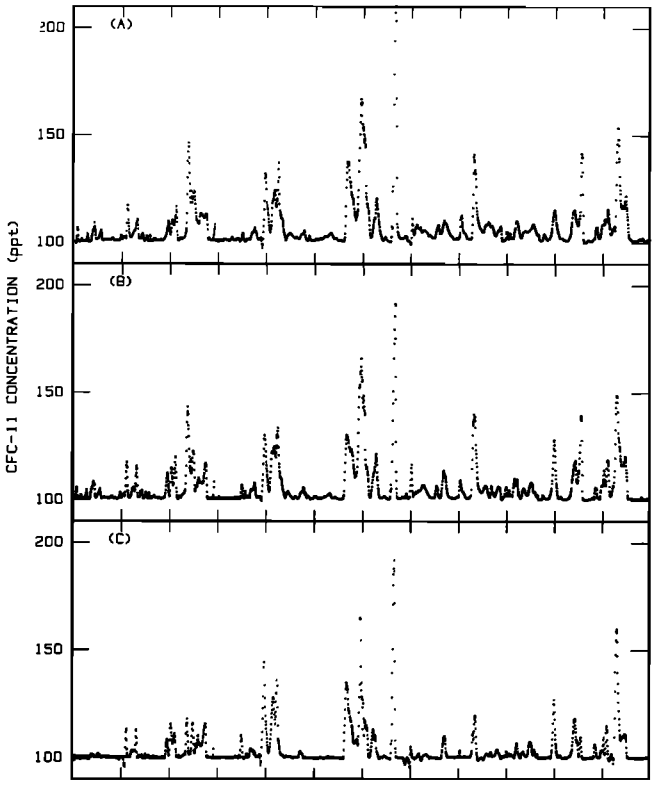

Fig. 16. Time series of CFC-11 surface concentrations simulated by the CTM at the Adrigole site. Background concentrations are maintained at 100 ppt by the boundary conditions surrounding the European window. (*a*) Results from the 4° × 5° CTM, using second-order moments for both sources and transport. (*b*) Results from 4° × 5° resolution, using the slopes scheme for transport and the 4° × 5° source grid without moments. (*c*) Concentrations calculated by the 4° × 5° CTM, with second-order moments but with the original 8° × 10° source grid. (*d*) Results from the 8° × 10° CTM, using the slopes scheme. Simulated time series are shown for (*e*) the Canary Islands and (*f*) central Germany from the calculation described for Figure 16*a*.

from 120×10^6 to 140×10^6 kg yr^{-1}. The 8° × 10° CTM (dotted line, time series in Figure 16*d*) produces substantially lower covariances than observed near $\Delta = 0$ but produces higher variances at $\Delta = 10$ days. This pattern is consistent with the premise that coarse resolution results in less-intense pollution events of longer duration. Covariances from the 4° × 5° CTM are shown for both the standard slopes method (dashed line, time series in Figure 16*b*) and the second-order moments method (solid line, time series in Figure 16*a*). Both of these simulations result in pollution episodes which are statistically very similar to those observed at Adrigole. The 4° × 5° SOM simulation has more narrowly defined episodes than the 4° × 5° with first-order moments, producing variances which are 20% higher at the peak ($\Delta = 0$) and 20% lower on the shoulder ($\Delta = 4$ days); the autocovariance has a half-height half-width of 2 days and a shoulder extending to 10 days, in excellent agreement with the ALE observations.

The highest mixing ratios observed at Adrigole cannot be simulated with the current model. The most intense events have durations less than 8 hours; they correspond to air masses with horizontal scales of 100 km or less which would be diluted over a larger grid size in our model, even in the 4° × 5° SOM model. These events are likely to be plumes from major urban centers, contribute about 20% of the variance at the Adrigole site, and represent less than 5% of the observations [*Prather*, 1985].

4. Summary and Conclusions

The three-dimensional chemical tracer model incorporates geographic emission patterns and simulates the distributions of CFC concentrations over latitude, longitude, altitude, and time. We summarize the major findings as follows.

The three-dimensional distribution of CFCs makes it difficult to derive globally integrated quantities solely on the basis of data from surface stations. Background air from the boundary layer near northern mid-latitude continents contains, on average, more CFC than that found aloft. In general, use of observed surface concentrations of CFCs in the northern hemisphere tends to lead to an overestimate of the hemispheric abundance, while in the southern hemisphere the opposite behavior occurs. Prejudicial location of observing sites in the boundary layer near continental sources can result in further bias toward higher values. Systematic errors occur in spite of attempts to choose remote sites and the capability of the researchers to remove selectively the data corresponding to polluted air. These errors propagate when surface data are used to calculate interhemispheric differences. The model allows an accurate estimate of global burdens, using data from surface stations, cruises, or aircraft flights, by simulating the global distributions and providing a quantitative estimate of the influence of sampling bias.

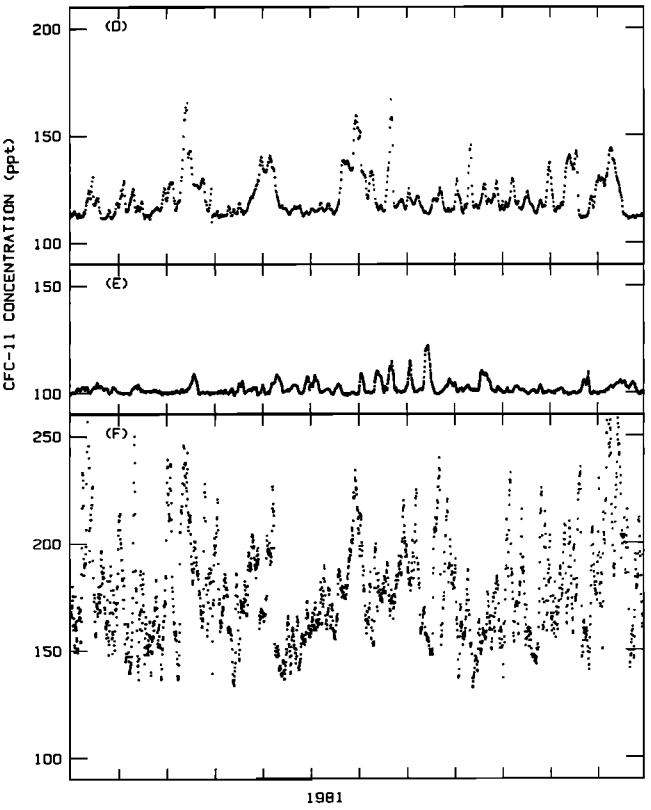

Fig. 16. (continued)

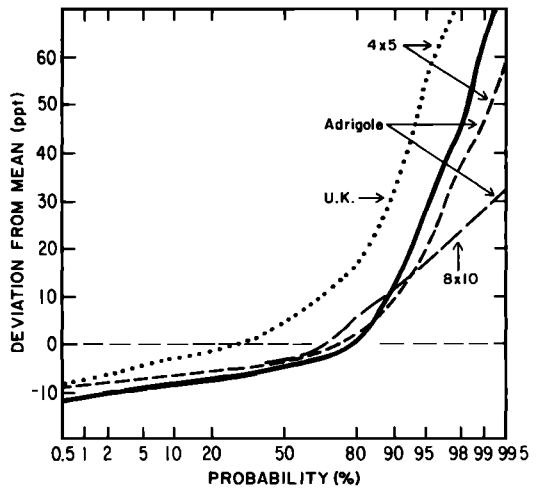

Fig. 17. Probability distribution of CFC-11 concentrations. The solid line shows the distribution of the ALE observations of CFC-11(*S*) at Adrigole after a least squares linear fit was removed. Modeled concentrations for the Adrigole grid square were treated similarly. Results are shown from the 8° × 10° global CTM (long-dashed line) and from the 4° × 5° window CTM with full SOM (short-dashed line). The grid square immediately to the east of Adrigole contains significant U.K. sources. Its probability distribution from the 4° × 5° SOM is included (dotted line), but in this case the reference mean is the average value from the Adrigole grid.

The model indicates that seasonal cycles in moist convection, with a maximum over the continents in summer, lead to an annual cycle in the surface concentration of compounds with a land source. In winter, when vertical mixing is weakest over land, concentrations peak near sources, and these high surface values are carried far downwind in the lower atmosphere. For example, during January, contributions from the European source of CFCs are blown into the Arctic, as shown by the surface contours in Figures 5 and 7. It is difficult at present to test the model's simulation of concentrations in air adjacent to or over a source region, since data records equivalent to the ALE series are scarce for polluted environments. Such data are clearly important as a benchmark in development of CTMs.

The model provides excellent simulation of synoptic-scale pollution episodes at observing sites 400–2000 km removed from major sources, Point Barrow and Adrigole, for example. The modeled climatology for Adrigole was statistically very similar to the observed climatology, provided that the highest-resolution model was used, i.e., 4° × 5° with SOM. Simulation of such sites requires high resolution for both sources and transports as well as time series analysis to characterize the distribution of observed concentrations, not just the mean. It appears that data from stations adjacent to source regions, in conjunction with the CTM, allow a direct estimate of regional rates of emission to the atmosphere. The model can be used to predict trace gas climatologies for projected monitoring sites.

Parameterized diffusion, to mimic mixing in the horizontal dimension associated with deep vertical convective activity, was introduced and adjusted to match the interhemispheric exchange observed for CFC-11. It had little impact on intrahemispheric transport but resulted in an increase of 50–100% in the rate for cross-equatorial transport. The parameterization gave an excellent simulation of the north-south distribution of ^{85}Kr as well as CFCs.

Interhemispheric transport in this model is manifest primarily by extensive exchange in the upper tropical tropo-

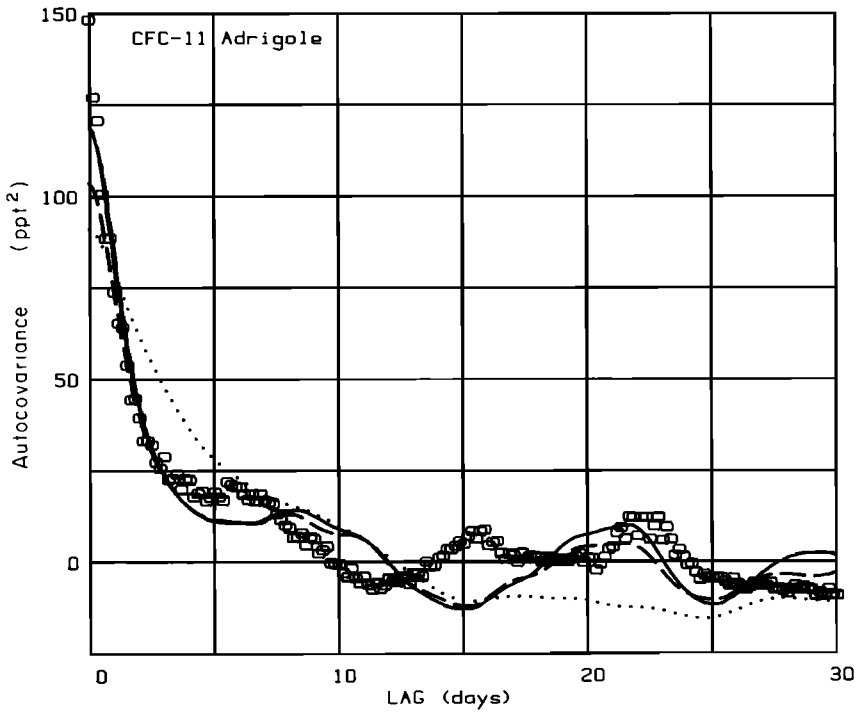

Fig. 18. Autocorrelations of CFC-11 at Adrigole, Ireland. The ALE data (open circles) have had a linear trend removed, and the lowermost and uppermost 1% of all values have been truncated to the first and ninety-ninth percentile values, respectively. The simulated concentrations from the CTM have had the mean concentrations removed. Autocorrelations are shown for the 8° × 10° resolution using the slopes scheme (dotted line), 4° × 5° resolution using the slopes scheme (dashed line), and 4° × 5° resolution using second-order moments for both transport and sources (solid line).

sphere. The predominant flux of CFCs into the southern hemisphere occurs above 400 mbar. In the northern tropics the vertical profile of CFCs falls off with altitude from the surface, while in the southern tropics the profile reverses and increases with altitude. Observational definition of the latitudinal distribution of CFCs from the planetary boundary layer to 200 mbar could aid in understanding interhemispheric transport and in refining treatment of this process in the CTM.

APPENDIX A: DYNAMICAL MODEL

The essential features of the dynamical model are described by *Hansen et al.* [1983] and will be reviewed only briefly here. We used the high-resolution (4° latitude × 5° longitude) version of the GISS GCM, with 72 elements in longitude, 46 in latitude, and nine layers in the vertical. The model uses σ coordinates [*Phillips*, 1957], with an upper boundary at a pressure of 10 mbar, as shown in Figure A1. Dynamical variables are calculated according to the prescription of *Arakawa*'s [1972] *B*-grid, with horizontal winds (u, v) evaluated at the corners of the grid. The surface pressure p_s, potential temperature, geopotential height, and specific humidity are calculated at the centers of grid elements.

The boundary conditions assume that there is no vertical flux of mass across either the upper (10 mbar) or lower (surface) boundaries. Temperatures at the sea surface are specified seasonally on the basis of observations. Temperatures at the land surface are calculated with an energy balance model, allowing for diurnally varying insolation, radiative and conductive exchange of heat with the atmosphere, storage of heat and moisture in two ground layers, evaporation of H_2O, and the possible presence of snow and ice.

Convection is predicted to occur under circumstances where the computed temperature profile is unstable with respect to vertical motion. The model recognizes two types of convection, wet and dry. If the moisture content of the unstable layer is large enough to allow condensation following vertical motion, half of the material in the layer is moved upward along a moist adiabat to the point where its density attains equilibrium with the environment. The transported mass is then deposited in the upper layer. Uniform subsidence is assumed elsewhere in the grid element to balance the upward flux of mass associated with convection. If the moisture content of the unstable layer is insufficient for condensation, vertical motion proceeds on a dry adiabat until the level of stability is reached; complete mixing of layers is assumed along this path.

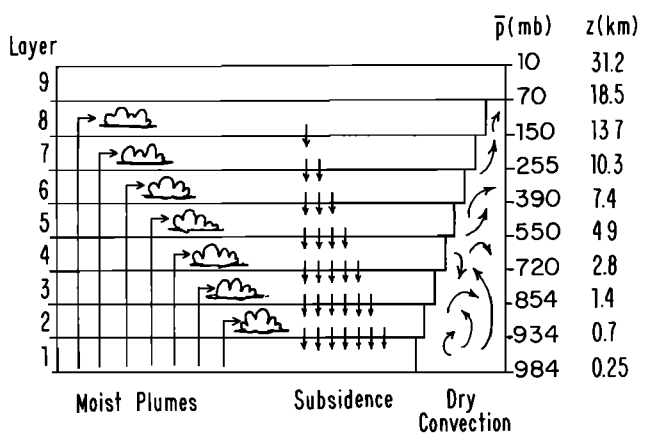

Fig. A1. Vertical coordinates of the CTM/GCM, showing processes included in moist and dry convection. The GCM has a horizontal resolution of 4° latitude by 5° longitude. The pressures shown assume a surface pressure of 984 mbar, the global average from the GCM. Altitudes corresponding to these pressures are taken from U.S. Standard Atmosphere (1976).

Moist convection is associated with formation of thick cumulus clouds. The cumulus clouds are assumed to extend throughout grid points for which condensation is expected. They account statistically for about 10% of the global cloud cover. Clouds in the model are more commonly associated with vertical motions and supersaturation on larger scales. Large-scale clouds are treated on a probability basis. The chance that a cloud occurs within a given grid element is described by a probability distribution which depends on the temperature variance and the local relative humidity. This function is sampled randomly and gives a larger chance for cloud cover as the relative humidity increases. Clouds, if they occur, are assumed to cover a grid square completely [see *Hansen et al.*, 1983].

The primitive equations are solved numerically, using a second-order difference scheme with a combination of implicit and explicit time steps adding up to 1 hour. The physical state of the model (temperatures, surface conditions, moist and dry convection, cumulus precipitation) is updated hourly. The radiation budget, cloud cover, and large-scale precipitation are evaluated every 5 hours, which allows for diurnal variation of insolation and the associated adjustment of the near-surface boundary layer. Horizontal fluxes of mass across the boundaries of grid elements are integrated over 4-hour periods and stored at 4-hour intervals on a history tape which serves as input to the CTM. Surface pressures for each 4-hour interval are recorded and are used in the CTM, together with the horizontal mass fluxes to compute the vertical velocity field.

The vertical redistribution of mass due to convective overturning has a major effect on the distribution of chemical tracers. To include it, we record the number of moist convective events, coupling all possible layer pairs which occur in a 5-day period. Ideally, one would calculate the redistribution of tracers by treating convective events on an individual basis, i.e., hourly. This procedure, however, would vastly increase the requirements for storage and handling of GCM data and was judged unnecessary. The technique adopted to reconstruct the influence of convection on tracers, discussed later, uses statistical information for 5-day intervals recorded by the GCM.

A typical photochemical application of the CTM requires, in addition to the dynamical variables, data on temperature, water vapor, and cloud cover. Some of these data are stored on a 4-hour basis; the balance are available as 5-day averages. The height of the surface layer which is mixed by dry convection is recorded with a temporal resolution of 4 hours, sufficient to define the diurnal cycle. Most of the above information is available with a spatial resolution of 4° × 5° for two sequential model years, April 1 to March 31. The GCM was initialized with climatolgical data on January 1 and run for 27 months. Details and interpretation of results from the early model runs are given by *Hansen et al.* [1983].

APPENDIX B: CHEMICAL TRACER MODEL

The chemical tracer model (CTM) solves continuity equations over a three-dimensional grid for a set of chemically

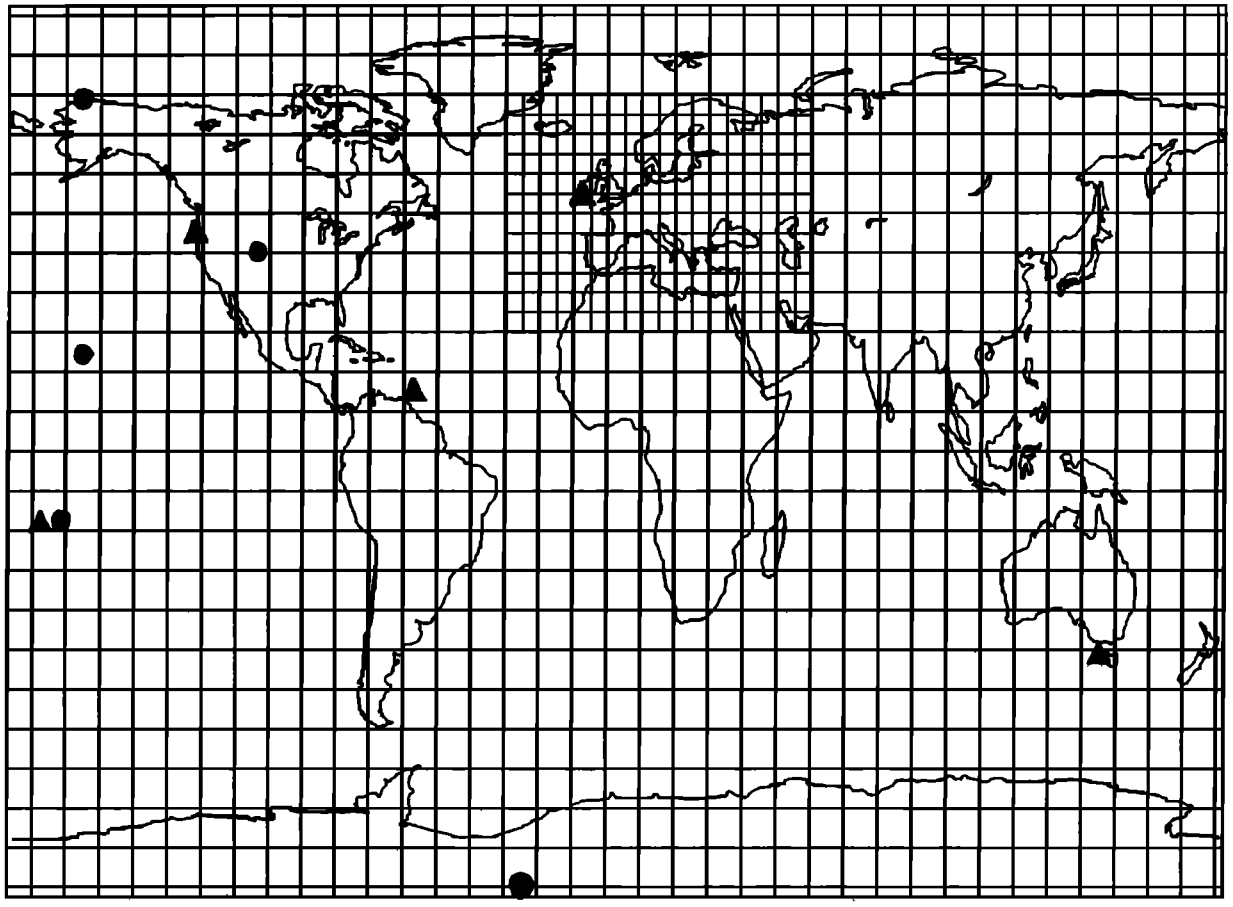

Fig. B1. Latitude-by-longitude grid of the 4° × 5°/8° × 10° global CTM, showing the finer resolution only for the European window. ALE sites are denoted by solid triangles, and GMCC sites (used for CFC analysis) are shown as solid circles.

reactive tracers. The present model augments procedures introduced by *Russell and Lerner* [1981]. It incorporates a revised first-order advection scheme, adding a second-order moments method for transport [*Prather*, 1986] allowing calculations to be carried out at high resolution on a limited "window" of the globe. Advection is treated over extended polar zones in order to improve numerical stability. A more detailed treatment of moist convection is incorporated. Photochemical losses in the stratosphere are properly accounted. A brief review of the basis for the model with a documentation of the added features follows.

B1. *The Three-Dimensional Grid*

The distribution of a trace gas is calculated at a discrete set of latitudes, longitudes, and pressures defining the grid boxes of the CTM. We carried out several calculations using a horizontal resolution of 4° × 5°, corresponding to the GCM's fine grid (as in the works by *Russell and Lerner* [1981] and *Hansen et al.* [1983]), 46 latitude zones, with boundaries at 4° intervals extending from 88°S to 88°N, and 72 longitudinal elements, from 177.5°W at 5° intervals to 177.5°E (see Figure B1). The vertical levels are defined by pressure according to the σ coordinates used in the GCM, as summarized in Figure A1. The vertical layers are bracketed by pressures of p_k^- and p_k^+, with k extending upward from 1 to 9. The pressure at the lower boundary of layer k is given (in millibar) by

$$p_k^- = \sigma_{k-1}(p_s - p_{top}) + p_{top} \tag{B1}$$

The pressure at the upper boundary of layer k (or, equivalently, at the lower boundary of layer $k + 1$) is given by

$$p_k^+ = \sigma_k(p_s - p_{top}) + p_{top} \tag{B2}$$

The local surface pressure p_s (in millibar) is calculated by the GCM. The pressure at the upper boundary of the GCM/CTM, p_{top}, is set equal to 10 mbar. Sources of tracer may be included at the lower boundary or in any grid box, but the upper boundary is treated as a rigid lid. Photochemistry above 10 mbar is included as an additional source or sink at the top of layer 9.

The average dimensions of grid box k at latitude θ are

$$\begin{aligned} \Delta X &= (\pi a/72)[\cos(\theta + 2°) + \cos(\theta - 2°)] && \text{for } \theta < 88° \\ \Delta X &= (\pi a/72)\cos(88°) && 88° < \theta < 90° \\ \Delta Y &= (\pi a/45) && \text{for } \theta < 88° \\ \Delta Y &= (\pi a/90) && 88° < \theta < 90° \end{aligned} \tag{B3}$$

and

$$\Delta p_k = (p_s - p_{top})(\sigma_{k-1} - \sigma_k)$$

Here ΔX defines the east-west extent of the box (in meters), ΔY refers to the north-south dimension (in meters), and a denotes the radius of the earth. The mass M_k of air contained in the grid box (in kilograms) is

$$M_k = (100/g)\,\Delta p_k\,\Delta X\,\Delta Y \tag{B4}$$

where $a = 6375000$ m and $g = 9.81$ m s^{-2}.

Many calculations were made with a subset of the 4° × 5° CTM, using a resolution of 8° × 10° with 24 latitude zones with 36 meridional elements. The same polar boxes and vertical layers were used, but four horizontal grid elements of the 4° × 5° model were combined into a single 8° × 10° box. Winds from the 4° × 5° GCM were integrated along the sides of the 8° × 10° box, and physical quantities (p_s, T, q) were averaged over the four 4° × 5° elements comprising the larger box. The relationship of these grids is shown in Figure B1. This formulation reduces computational time by about a factor of 8, enabling CFC simulations to extend to more than a decade of model time.

The fundamental quantities calculated and stored by the CTM are the air mass M, the tracer mass S and its first-order moments in three dimensions, S_x, S_y, and S_z (all in kilograms). The moments (or slopes, see *Russell and Lerner* [1981]) define the mixing ratio of tracer throughout the grid box as a combination of linear functions with respect to the mass distribution of air. The mean value of the mass mixing ratio over the entire air mass in the grid box ($\bar{r}$) is equal to the central value,

$$\bar{r} = r(\text{center}) = S/M \tag{B5}$$

and the values at the edges, when averaged over the other two dimensions, are given by

$$\begin{aligned} r(+\Delta X/2) &= (S + S_x)/M \\ r(-\Delta X/2) &= (S - S_x)/M \end{aligned} \tag{B6}$$

B2. *Advection*

Tracer is advected as a component of the east-west (U) and north-south (V) mass fluxes (in kilograms per second) across the sides of grid boxes, as averaged by the GCM over a period of 4 hours [see *Russell and Lerner*, 1981]. The fluxes of mass between two grid boxes in layer k are computed with the GCM winds,

$$\begin{aligned} U_k &= (100/g)\,\Delta p_k\,\Delta Y\,\bar{u} \\ V_k &= (100/g)\,\Delta p_k\,\Delta X\,\bar{v} \end{aligned} \tag{B7}$$

where $\bar{u}$ (in meters per second) is the mean of the two zonal winds at the corners of the GCM's B-grid which define the boundary between adjacent CTM grid boxes, and $\bar{v}$ (in meters per second) is the mean of the two meridional winds. The vertical flux of mass (W) (in kilograms per second) in a specific grid box is calculated from the change in mass due to the local horizontal convergence in the layer and the overall pressure tendency. The latter gives the change in mass of the total column at a grid element (M) as a function of the change in pressure over the time step Δt and is calculated from the total convergence.

$$\begin{aligned} M(\Delta t) - M(0) &= (100/g)[p_s(\Delta t) - p_s(0)]\,\Delta X\,\Delta Y \\ &= \Delta t \sum_{k=1}^{k=9} (U_k^- - U_k^+ + V_k^- - V_k^+) \end{aligned} \tag{B8}$$

Horizontal fluxes of mass into layer k on the west and south faces are denoted by U_k^- and V_k^-, respectively; those out of layer k on the east and north faces are given by U_k^+ and V_k^+, respectively. The mass flux into box k across the lower surface, W_k^-, is derived then from three terms,

$$\begin{aligned} W_k^- = W_k^+ &- (U_k^- - U_k^+ + V_k^- - V_k^+) \\ &- (\sigma_{k-1} - \sigma_k)[M(\Delta t) - M(0)]/\Delta t \end{aligned} \tag{B9}$$

where W_k^+ ($= W_{k+1}^-$) is the upward mass flux (in kilograms per second) out the top of the box. The Ws are calculated for each layer from the top downward with the upper boundary condition

$$W_{k=9}^+ = 0 \tag{B10}$$

Advection of tracer is always from the upstream direction. In most global calculations we used the first-order moments (slopes) method. Let a mass flux U advect a portion of the upstream box (shown by the superscript "up") into the central box for a time interval Δt. The mass and moments of the advected air parcel are

$$\begin{aligned} \Delta M &= U\,\Delta t = \alpha M^{\text{up}} \\ \Delta S &= \alpha S^{\text{up}} + \alpha(1-\alpha) S_x^{\text{up}} \\ \Delta S_x &= \alpha^2 S_x^{\text{up}} \\ \Delta S_y &= \alpha S_y^{\text{up}} \\ \Delta S_z &= \alpha S_z^{\text{up}} \end{aligned} \tag{B11}$$

where α is the upwind Courant number, $U\Delta t/M^{\text{up}}$. The increments from equation (B11) are combined with expressions for the tracer and air mass already present in the grid box to yield new mass and moments,

$$\begin{aligned} M^{(\text{new})} &= M + \Delta M \\ S^{(\text{new})} &= S + \Delta S \\ S_x^{(\text{new})} &= [MS_x + \Delta M \Delta S_x + 3(S\Delta M - M\Delta S)]/(M + \Delta M) \\ S_y^{(\text{new})} &= S_y + \Delta S_y \\ S_z^{(\text{new})} &= S_z + \Delta S_z \end{aligned} \tag{B12}$$

The mass and moments remaining in the upstream box are then

$$\begin{aligned} M^{\text{up(new)}} &= (1-\alpha) M^{\text{up}} \\ S^{\text{up(new)}} &= (1-\alpha) S^{\text{up}} - \alpha(1-\alpha) S_x^{\text{up}} \\ S_x^{\text{up(new)}} &= (1-\alpha)^2 S_x^{\text{up}} \\ S_y^{\text{up(new)}} &= (1-\alpha) S_y^{\text{up}} \\ S_z^{\text{up(new)}} &= (1-\alpha) S_z^{\text{up}} \end{aligned} \tag{B13}$$

A more accurate scheme for advection of tracers has been implemented as an alternative numerical method in the CTM and is used where we wish to obtain the finest effective resolution. This method is based on conservation of the second-order moments of the tracer distribution in each grid box. The method is an extension of the slopes scheme (equations (B11)–(B13)) and improves the effective spatial resolution by more than a factor of 2 in all dimensions. The greater requirements for storage (factor of 3) and computational time (factor of 2)

are modest when compared to the typical increases in both storage and computational time (factors of 8) associated with a straigthforward doubling of the horizontal resolution. (See *Prather* [1986] for derivation of the method and for formulae equivalent to equations (B11)–(B13)). Several studies were performed using both of these numerical methods, as discussed in section 3.3.

The method of tracer advection described above is formulated for motion along a single dimension, and three-dimensional motion is treated with successive application of the method in different directions, as discussed by *Russell and Lerner* [1981]. For a basic time step of 4 hours we have optimized the sequence of advective computations as $U + V + W + U + V + U + W + V + U$, with time steps of 1, 4/3, and 2 hours for the U, V, and W steps, respectively. The time steps for each dimension were chosen by the global value of the Courant number in each dimension (i.e., $U\Delta t/M < 1$) for the GCM wind fields. Advantages of separating the motions thus include both simplified formulae for advection (equations (B11)–(B13) and the ability to take larger time steps in alternate dimensions. The sequencing of the U, V, and W calculations was chosen to be as symmetrical as possible [after *Russell and Lerner*, 1981] in order to minimize errors associated with this forward-Euler (versus trapezoidal) integration of the advective transports. The symmetry also maintains a mass distribution after each step which most closely follows that resulting from the simultaneous, three-dimensional air motions. The dimensionally separate integration of the continuity equation is stable and accurate for the upstream methods used here (see Russell and Lerner's spatial leap-frog scheme [*Russell and Lerner*, 1981]), in part because grid boxes are allowed to retain extra air and tracer mass during intermediate steps. The content of each box is not tied to its physical dimensions until the end of the overall time step, when (B4) should apply.

Ideally, the horizontal convergence of mass computed with the assumed wind fields should allow the change in surface pressure to be predicted, using (B8) and (B9). However, the CTM and GCM use different numerical schemes, and the GCM applies a nonlocal zonal filter to surface pressures. After an advective step there will be a pressure error,

$$p_s^{\text{err}} = p_s(\text{CTM}) - p_s(\text{GCM}) \qquad \text{(B14)}$$

associated with each column of grid boxes in the CTM. In practice, the air mass calculated by the CTM differs only slightly (less than three parts in 1000) from that predicted by the GCM. In the earlier version of the CTM the air mass was reset according to (B4) in each grid box at the end of each 4-hour time step with the surface pressures recorded from the GCM. For the mass-conserving scheme outlined earlier, this procedure produced noise in the tracer mixing ratios of the order of 0.6 ppt out of 200 ppt.

We have developed an alternative method, a pressure filter for the CTM, in which the surface pressures computed by the CTM are constrained to track the pressures determined by the GCM. A separate horizontal wind field is calculated so that the mass flux between adjacent grid boxes removes one-eighth of the difference in the pressure error between neighboring grid squares. The northward flux from grid (i, j) to its neighbor $(i, j + 1)$ is given by

$$V^p = 0.125[p^{\text{err}}(i, j) - p^{\text{err}}(i, j + 1)](100/g)\ \Delta X\ \Delta Y/\Delta t \qquad \text{(B15)}$$

and the eastward flux is calculated similarly between adjacent grid boxes in the zone,

$$U^p = 0.125[p^{\text{err}}(i, j) - p^{\text{err}}(i + 1, j)](100/g)\ \Delta X\ \Delta Y/\Delta t \qquad \text{(B16)}$$

A global advection step using fluxes (U^p, V^p) is computed at the end of each dynamical time step, every 4 hours for the 4° × 5° CTM.

Pressure filtering will not guarantee exact agreement between the CTM and GCM for each time step but does maintain pressure fields in the CTM, which differ from the GCM typically by less than 5 mbar (rms) after 1 year's integration. Use of the pressure filter had no significant effect on the results obtained for CFCs with the present combination of GCM/CTM, except for simulations of the variability expected at large distances from sources, such as over Antarctica. The pressure filter becomes an essential component of the CTM if the wind field is noisy. For example, observed wind fields with errors of ± 0.5 m s^{-1} may lead to divergence from the observed pressure fields by ± 90 mbar d^{-1} on a 4° × 5° grid.

Our method for solving the three-dimensional continuity equations is often called operator splitting or alternating directions [e.g., *Dahlquist and Bjorck*, 1974]. It is applied consistently in the CTM for the various processes affecting trace gases: advection moves the tracer for a 4-hour period, convection vertically distributes tracer mass for the same interval, tracer from sources during the 4-hour period is added to each box, and tracer is removed allowing for local chemical loss.

B3. *Windows*

Study of the dispersal of gases from source regions on continents requires the finest resolution attainable in the model, while much lower resolution may often be appropriate for global simulations. We designed the CTM so that high-resolution calculations of tracer concentrations could be carried out using a restricted rectilinear subset, or window, of the global latitude-by-longitude grid. The winds and convection patterns are identical to those used in the full global model. Boundary conditions for the tracer are imposed at all layers along the edges of the window. Since tracer advection is treated using an upstream method, we chose to specify the mixing ratio of tracer in air which enters a particular window. In case studies of source regions, the United States or Western Europe, for example, the upwind boundaries were placed over the oceans, well away from continental sources. We are able thus to specify background mixing ratios at the upstream boundaries, using results for the CTM global run. Studies discussed in this paper demonstrate that results in the interior of the window are insensitive to the somewhat artificial treatment of the boundaries. Use of a window option results in considerable savings, more than a factor of 10, when compared with global studies of similar resolution. Simulation of time series for CFCs at Adrigole, Ireland, was performed using a window calculation for Europe, with the window located as shown in Figure B1.

B4. *Extended Polar Zones*

Extended zones near the poles can be defined so that the CTM grid allows nearly equivalent areas for the high-latitude grid-boxes, as shown in Table B1. This approach leads to numerical advantages similar to those attained with the equal-area grid employed at GFDL [*Mahlman and Moxim*, 1978]

TABLE B1. Extended Polar Zones

Index	Latitude, °N	Area, 10^{10} m^2	Extended Zone Number	Extended Zone Area, 10^{10} m^2
		4° × 5° Grid		
46	90	0.2	72	15.5
45	86	1.7	16	27.5
44	82	3.4	8	27.5
43	78	5.1	4	20.5
42	74	6.8	4	27.2
41	70	8.4	2	16.9
40	66	10.0	1	10.0
39	62	11.6	1	11.6
38	58	13.1	1	13.1
37	54	14.5	1	14.5
36	50	15.9	1	15.9
35	46	17.1	1	17.1
34	42	18.3	1	18.3
33	38	19.4	1	19.4
32	34	20.5	1	20.5
31	30	21.4	1	21.4
30	26	22.2	1	22.2
29	22	22.9	1	22.9
28	18	23.5	1	23.5
27	14	23.9	1	23.9
26	10	24.3	1	24.3
25	6	24.5	1	24.5
24	2	24.7	1	24.7
		8° × 10° Grid		
24	90	0.4	36	15.5
23	84	10.3	4	41.2
22	76	23.8	2	47.7
21	68	36.9	1	36.9
20	60	49.3	1	49.3
19	52	60.7	1	60.7
18	44	70.9	1	70.9
17	36	79.7	1	79.7
16	28	87.0	1	87.0
15	20	92.6	1	92.6
14	12	96.4	1	96.4
13	4	98.3	1	98.3

and with the rhomboidal truncation method used in spectral models [*McAvaney et al.*, 1978], such as the NCAR Community Climate Model. We combine several adjacent grid boxes along a latitude circle for the east-west advection, more than doubling the Courant limit on the time step. Longer time steps may be used without sacrificing stabilty or accuracy.

The use of extended zones is limited to the advective calculation; the CTM always stores tracer moments and performs diagnostics on the basic grid (e.g., 5° longitude). Application of extended zones is different for advection in each dimension. For east-west transport the N individual grid boxes are combined into an extended polar zone (superscript epz) by the following formulae, which preserve the first- and second-order moments of the tracer distribution:

$$S^{epz} = \sum_{i=1}^{N} S^i \qquad \text{also } S_y, S_z, S_{yy}, S_{zz}, \text{ and } S_{yz} \tag{B17a}$$

$$NS_x{}^{epz} = \sum_{i=1}^{N} [S_x{}^i + 3(2i - N - 1)S^i] \tag{B17b}$$

$$NS_{xy}{}^{epz} = \sum_{i=1}^{N} [S_{xy}{}^i + 3(2i - N - 1)S_y{}^i] \qquad \text{also } S_{xz} \tag{B17c}$$

$$N^2S_x{}^{epz} = \sum_{i=1}^{N} \{S_{xx}{}^i + 5(2i - N - 1)\, S_x{}^i + 5[6i(i - N - 1) + (N + 1)(N + 2)]\, S^i\} \tag{B17d}$$

Advection of tracer is calculated using only the u winds at the ends of each extended zone. After completion of east-west advection, the extended polar zones are then repartitioned into the individual, equal-mass grid boxes by the inverse formulae which preserve the second-order moments:

$$S^i = S^{epz}/N + S_x{}^{epz}(2i - N - 1)/N^2 + S_{xx}{}^{epz}[6i(i - N - 1) + (N + 1)(N + 2)]/N^3 \tag{B18a}$$

$$S_x{}^i = S_x{}^{epz}/N^2 + S_{xx}{}^{epz}3(2i - N - 1)/N^3 \tag{B18b}$$

$$S_{xx}{}^i = S_{xx}{}^{epz}/N^3 \tag{B18c}$$

$$S_{xy}{}^i = S_{xy}{}^{epz}/N^2 \qquad \text{also } S_{xz} \tag{B18d}$$

$$S_y{}^i = S_y{}^{epz}/N + S_{xy}{}^{epz}(2i - N - 1)/N^2 \qquad \text{also } S_z/S_{xz} \tag{B18e}$$

$$S_{yz}{}^i = S_{yz}{}^{epz}/N \qquad \text{also } S_{yy}, S_{zz} \tag{B18f}$$

North-south advection in the CTM is complicated by the nesting of extended zones as one approaches the poles. The size of the extended zone used in transport is limited by the latitude belt which lies closest to the equator. For example, before computing north-south advection between the belts at 78°S ($N = 4$) and 82°S ($N = 8$), both latitude belts are grouped into matching zones of $N = 4$ according to (B17). The meridional mass fluxes V are summed across the interface between the matching zones. After advection the two zones are repartitioned according to (B18).

Vertical advection is computed by summing the mass fluxes W over the grid boxes comprising the extended zone, by computing transport for the combined zone (equation (B17)), and by repartitioning tracer into individual grid boxes (equation (B18)). Under some circumstances, vertical winds from the GCM exhibit high-frequency signals near the pole: large upward fluxes in one grid box are matched by corresponding downward fluxes in adjacent boxes. Use of extended polar zones is equivalent to a polar filter; mean winds are unchanged, but high-frequency artifacts in the vertical winds are suppressed.

B5. *Convection*

The GCM calculates convection hourly and saves the pattern averaged over a period of H hours, where H ranges from 120 (5 days) to 720 (1 month). The number of moist convective events, as sampled by the GCM every hour over this period, is $n_{km}{}^{wet}$ for convection beginning in layer k and ending in layer m.

Layer 7 is the upper limit for participation in any type of convection in the CTM. Each such event is assumed to take 50% of the mass in layer k and deposit it in layer m. The choice of 50% for the participating mass is adopted from the parameterization of the GCM. (Numerical experiments have shown that the total convective transport in the GCM is only slightly sensitive to the values adopted for this fraction, since the total convective flux responds in first-order to the energy balance of the model. Hence a smaller fraction results in more frequent convection.)

For moist convection we calculate $0.50n_{km}{}^{wet}/H$ as the average fraction of the mass in layer k which is convected to

layer m during the GCM's 1-hour time step over this averaging period (H). The fraction of the box involved in convection during the basic CTM time step of T hours is then

$$c_{km}^{\text{wet}} = 1 - (1 - 0.50 n_{km}^{\text{wet}}/H)^T \tag{B19}$$

The amount of tracer transported by moist convection is given by (B4), (B5), and (B19):

$$\Delta S^{km} = S^k \, c_{km}^{\text{wet}} \tag{B20}$$

If the tracer is soluble or chemically reactive within a cloud, a fraction of ΔS^{km} may be removed before it is deposited in layer m.

Similarly, the statistics for dry convection record the number of hourly intervals (n_{km}^{dry}) for the averaging period of H hours during which the GCM predicted that complete mixing occurred between layers k and m. In this case we calculate the fraction of the grid box involved during a time step of T hours as

$$c_{km}^{\text{dry}} = 1 - (1 - n_{km}^{\text{dry}}/H)^T \tag{B21}$$

The mixing of tracer is calculated by summing the amount of tracer mass (proportional to the air mass) involved in dry convection which originates in layer k,

$$\sum_{j=k}^{7} \left[S^j \sum_{m=j}^{7} c_{km}^{\text{dry}} \right] \qquad c_{kk}^{\text{dry}} \equiv 0 \tag{B22}$$

and redistributing it over layers k through 7 in proportion to the amount of air mass participating from each grid box. All information about vertical slopes in convecting parcels is lost ($S_z = 0$), but horizontal slopes are summed as in (B22) and retained by the CTM.

Because long time steps ($T > 1$) may lead to unrealistic extrapolation of convection frequencies, limits are placed on the maximum participation in wet or dry convection originating from any one layer,

$$\begin{aligned} \sum_{m=k+1}^{7} c_{km}^{\text{wet}} &< 0.80 \\ \sum_{m=k+1}^{7} c_{km}^{\text{dry}} &< 0.80 \end{aligned} \tag{B23}$$

and the values of c_{km} in a vertical column are scaled linearly to meet this restriction if required.

The transport of tracer by moist convection (i.e., a plume reaching directly from layer k to layer m) is balanced by a downward subsidence of air and tracer within the same column of grid boxes (as in the work by *Russell and Lerner* [1981]). Subsidence is treated as the flow of air from the bottom of one layer (k) into the top of the layer below. This downward flow is treated as a negative advective flux,

$$W_k^{\text{wet}} = -\sum_{m=k}^{7} \left(\sum_{j=1}^{k-1} M^j \, c_{jm}^{\text{wet}} \right) \tag{B24}$$

which transports tracer using the vertical moments in the same manner as in regular vertical advection. The mass of tracer moved upward in the plume is independent of the vertical slope S_z in the originating grid box, loses all memory of that slope, but may retain information about the horizontal moments (S_x, S_y) when it reaches layer m.

B6. *Convective Diffusion*

The GCM's treatment of convection assumes implicitly that horizontal mixing occurs over some scales intermediate between that of the moist convective plumes and that of the explicitly resolved grid. The complete cycle of convection may be viewed schematically as follows: air enters the convective cell, is rapidly raised to the top of the cell, spreads out, and descends slowly to the lower levels of the atmosphere where the cycle repeats. By conservation of mass the area of descending air scales as the mass flux in the convective plume divided by the vertical velocity of the descending air. The area of this mesoscale system and the rate at which air passes through it determine the extent of horizontal mixing. This circulation is explicitly resolved in two-dimensional, nonglobal chemical models of these cloud systems [*Gidel*, 1983; *Chatfield and Crutzen*, 1984]. Unfortunately our global model cannot resolve these mesoscale systems, and we must average the advective transports of tracers in these systems, approximating the mean transports by eddy diffusion.

The GCM has not explicitly included this diffusion, and we shall argue that its effect on the dynamics is small but that its impact on chemical tracers with gradients across the equator is significant, even for small amounts of diffusion. In this paper we use CFCs to understand what levels of mesoscale mixing are plausible, to place limits on the role of subgrid diffusion which might be incorporated into the GCM.

Shallow convection involving many small convective cells, such as boundary-layer cumulus, is expected to mix tracer over horizontal scales of only a few kilometers. However, deep organized convection, as seen in convective complexes, may have horizontal scales of several hundred kilometers [*Zipser*, 1969]. We therefore allow horizontal diffusion to be associated with the convergence of air into deep convective updrafts. We define deep convection to originate in layers 1–4 and to extend to three or more layers above. The number of hourly convective events is weighted (arbitrarily) by the depth of vertical motion, $(m - k)/3$, and a horizontal diffusion coefficient

TABLE B2. Zonal Average of Convective Diffusion for Scale Length D = 250 km

Latitude, deg	Dec.-Jan.-Feb.	March-April-May	June-July-Aug.	Sept.-Oct.-Nov.	Annual Average
84	0	0	0	0	0
76	2	1	1	2	2
68	12	7	21	12	13
60	26	15	36	22	25
52	29	27	42	26	31
44	39	38	45	36	40
36	53	47	61	71	58
28	21	27	70	70	47
20	55	49	84	102	72
12	184	137	132	145	149
4	156	148	145	148	149
−4	128	159	144	125	139
−12	124	129	96	109	115
−20	99	74	32	46	63
−28	55	64	63	32	54
−36	37	71	103	63	69
−44	29	51	62	39	45
−52	18	35	37	23	29
−60	5	18	11	7	10
−68	3	4	1	1	2
−76	7	0	0	1	2
−84	7	0	0	1	2

Diffusion is given in units of 10^4 m^2 s^{-1}.

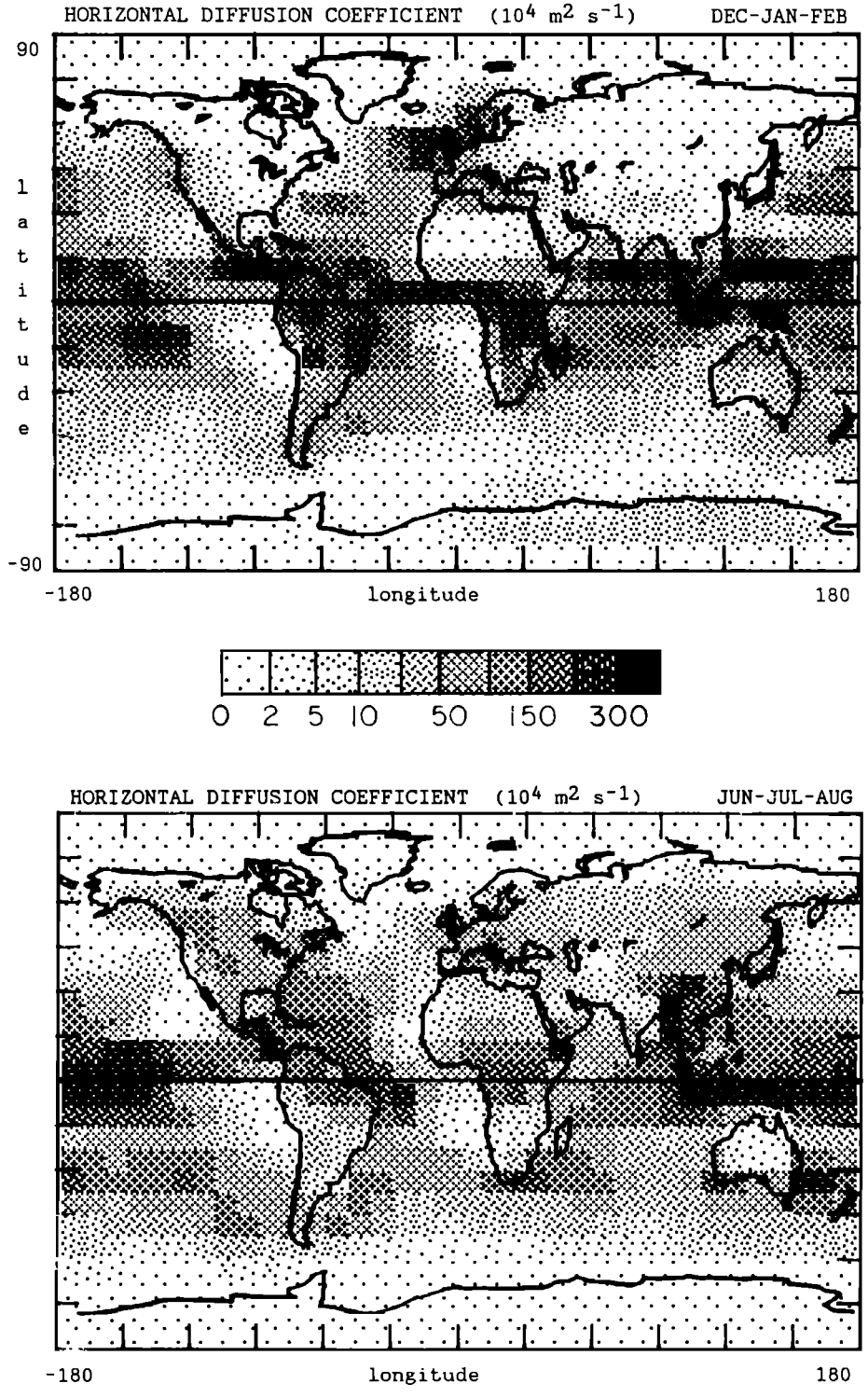

Fig. B2. Diffusion coefficients associated with moist convection are shown for the average of northern winter (December-January-February) and summer (June-July-August). The diffusion coefficients are in units of 10^4 m^2 s^{-1} and correspond to D = 250 km (see text).

K (in square meters per second) is calculated from the convective frequency and a length scale D:

$$K = D^2 \sum_{k=1}^{4} \left[\sum_{m=k+3}^{m=7} (0.5\, n_{km}{}^{\text{wet}}/H)(m-k)/3 \right] \quad \text{(B25)}$$

Horizontal diffusion, like convection, is limited to layers 1 through 7 and applied equally to all layers. For a large region of uniform convective activity, the formulation of K is indepenent of grid size. It is, however, directly proportional to the relative mass flux per event, currently 50%.

The change in the amount of tracer in box i due to diffusive mixing with the adjacent box $(i + 1)$ is calculated for the x

dimension as

$$\Delta S(i)^{\text{diff}} = \frac{[K_x(i) + K_x(i+1)]\Delta t}{2\,\Delta X^2}\,\frac{M(i) + M(i+1)}{2}$$

$$\cdot [S(i+1)/M(i+1) - S(i)/M(i)] = -\Delta S(i+1)^{\text{diff}} \qquad \text{(B26)}$$

where Δt is the time step and other symbols have been defined previously. Note that diffusive transport is calculated only from the zeroth moments; however, higher-order moments in the x direction are reduced by a factor corresponding to the extent of horizontal mixing,

$$\Delta S_x/S_x = -2K_x\Delta t/(\Delta X)^2 \qquad \text{also } S_{xx},\ S_{xy},\ S_{xz} \qquad \text{(B27)}$$

The diffusion process is calculated analogously for the y dimension, using $K_y = K_x = K$ from (B25).

We have assumed in this paper that any inadequacies in the rate of interhemispheric transport may be assigned to mesoscale mixing. The value of the parameter D was derived from the results of several CTM experiments with CFC-11, as described in section 2. Optimal simulations of the CFC global distribution and, in particular, of the interhemispheric difference were obtained from models using D in the range 180–250 km. The same range for D also provided excellent simulation of the latitudinal gradients observed for ^{85}Kr over the Atlantic [*Jacob et al.*, this issue].

Subgrid-scale diffusion has been incorporated into many three-dimensional tracer studies. For example, the GFDL model [*Levy et al.*, 1982] incorporates diffusion coefficients chosen to be proportional to the deformation of the wind field and, sometimes, proportional to the local gradient of tracer concentration [*Mahlman and Moxim*, 1978]. It is difficult from the published studies to determine the effective values of K used by these authors, but in regions of large wind shear (10 m s^{-1} across a 250-km grid) a typical value should be about 10^6 m^2 s^{-1}. This value is comparable to the zonal mean for K in the present study which peaks at about 1.5×10^6 m^2 s^{-1} in the tropics if D is taken as 250 km (see Table B2) or at about 8×10^5 m^2 s^{-1} for $D = 180$ km. The geographical distribution of K is shown in Figure B2. The influence of horizontal diffusion is confined in the present model mainly to low latitudes (see discussion of Figure 4), since deep convection is most common in the tropics where other mechanisms for tracer dispersion are relatively weak.

A first-order estimate of the impact of this parameterized diffusion on the GCM may be made by scale analysis as in the work of *Holton* [1972, p. 29]. We select momentum as the quantity with the largest gradient across the equator [see *Hansen et al.*, 1983]. The terms which dominate the momentum equation (advection, Coriolis, pressure) have magnitudes greater than or of the order of 10^{-4} m s^{-2}. By including a diffusion term in the scaled momentum equation,

$$\Delta u/\Delta t \sim 3 \times 10^{-4} + K\Delta u/(\Delta X)^2 \qquad \text{(B28)}$$

a first-order effect is found only for $K > 10^7$ m^2 s^{-1}. Thus the effects of our parameterized diffusion might be felt directly only near the one or two grid squares with $K \sim 3 \times 10^6$ m^2 s^{-1} (see Figure B2). The scaling argument cannot rule out other, more subtle effects on the circulation, and we are currently studying the impact of the subgrid diffusion by incorporating this parameterization (equation (B25)) in the General Circulation Model.

APPENDIX C: CHLOROFLUOROCARBON SIMULATIONS

Numerical simulation of the global distribution of CFCs requires a time integration of the Chemical Tracer Model with a particular history of emissions. We present here the scenario adopted to describe the release pattern of CFCs, the approach used to model removal in the stratosphere, the method adopt-

TABLE C1. CFC Release Scenario (1940–1982)

Year	CFC-11 Release, 10^6 kg yr^{-1}	CFC-11 Concentration,* pptv	CFC-12 Release, 10^6 kg yr^{-1}	CFC-12 Concentration,* pptv
1940†	0.3	0	7.3	0
1941	0.1	0	3.0	1
1942	0.1	0	3.7	1
1943	0.2	0	4.5	1
1944	0.2	0	6.1	1
1945	0.3	0	8.0	2
1946	0.6	0	13.9	2
1947	1.3	0	21.3	3
1948	2.3	0	24.8	5
1949	3.8	0	26.6	6
1950	5.5	1	29.7	7
1951	7.7	1	32.8	9
1952	11.1	1	34.2	10
1953	15.1	2	38.5	12
1954	18.7	3	43.6	14
1955	23.2	4	49.1	17
1956	28.9	5	57.3	19
1957	32.4	7	65.2	22
1958	30.4	8	68.5	26
1959	31.2	9	76.7	29
1960	40.9	11	91.5	34
1961	52.6	13	102.6	38
1962	65.9	16	117.9	44
1963	80.6	19	138.0	50
1964	95.7	23	160.4	58
1965	109.1	28	181.2	67
1966	122.2	33	201.6	76
1967	138.8	39	227.8	87
1968	158.1	46	255.9	99
1969‡	183.7	53	285.9	112
1970	209.0	62	313.4	127
1971	229.7	71	337.5	143
1972	259.1	82	368.3	160
1973	296.5	94	408.1	179
1974	327.0	108	443.5	199
1975‡	318.3	120	434.6	219
1976	325.3	133	425.9	239
1977	313.7	146	410.3	257
1978	294.6	157	384.9	274
1979	276.1	167	388.4	291
1980	264.8	176	392.5	309
1981	264.3	185	412.2	327
1982	258.8	194§	422.8	345§

*Concentrations refer to mean tropospheric mixing ratios at the end of the year and are calculated from integrating the CFC 11/12 emissions. Including the reduced stratospheric abundances, CFC 11/12 are effectively mixed over 0.93/0.96 of the total atmosphere. Losses are calculated with a 1-year lag for assumed steady state lifetimes of 60/125 years. Units are parts per trillion by volume (pptv).

†Emissions are taken from *CMA* [1983] with cumulative release before 1940 included in that year. Extrapolation of Soviet growth beyond 1976, approximately 18% per year, is based on Borisenkov and Kazakov (1977).

‡Total CFC 11/12 used to initialize the CTM in January 1970 is $1162/2258 \times 10^6$ kg, and in January 1976 is $2631/4416 \times 10^6$ kg.

§Steady state lifetimes for CFC 11 of 75/100 years would increase mixing ratios at the end of 1982 to 199/204 pptv. Similarly, lifetimes of 145/172 for CFC 12 would result in 349/353 pptv.

TABLE C2*a*. Geographic Release Grid

		I																															
		180°W						90°W							0°						90°E												180°E
	J	1	2	3	4	5	6	7	8	9	10	11	12	13	14	15	16	17	18	19	20	21	22	23	24	25	26	27	28	29	30	31	32	33	34	35	36
90°N	24																																				
84°N	23														0	0	0												0							
	22							0	0	0		0	0	0	0	0	0					0				0			0	0	0			0			
68°N	21	0		0	0	0	0	0	0	0	0		0		0	0		0				0	0	0	0	0	0	0	0	0	0	0	0	0	0	0
	20			0	0	0	0	0	0	0		0	0		0						3†	1†	1‡	4‡	1‡	2‡	0	1‡	1‡	0	0	0	0	0	0	0	0
52°N	19						0	2*	0	0	1*	0	0	0					0	9†	9†	6‡	1‡	4‡	2‡	2‡	1‡	1‡	0	0	0	0	0	1‡		0	
	18							1*	1*	1*	1*	8*	8*							0	8†	3†	1‡	1‡		0		0	0	0	0	1‡	0	0			
35°N	17							5*	1*	2*	4*	7*							0	0				2‡	0	0	0	0	0	0	0	2‡	3†	3†			
	16								0	2*	1*	1*							0	0	0	0	1‡	0	0	0	0	0	0	0	0	1‡					
20°N	15									1‡	0	1‡						0	0	0	0	0	0	0	0		0	2‡		0		0				
	14										0		1‡						0	0	0	0	0	0				0		0		1‡				
4°N	13											0	0	0							0	0	0	0						0	0					
4°S	12											0	0	0	0	0					0	0	0							0	0	0		0		
	11											0	0	0	0	0					0	0	0										0	0		
20°S	10												0	0	0	1‡					0	0	0	0								0	0	0		
	9												0	0	1‡							0	2†									0	0	0	0	
36°S	8												0	1‡								0											0	2†		0
	7												0																						0
52°S	6												0																						
	5																																		
68°S	4												0											0	0	0		0	0	0	0	0	0	0	0	
	3				0	0	0	0	0	0	0	0	0	0			0	0	0	0	0	0	0	0	0	0	0	0	0	0	0	0	0	0	0	
84°S	2	0	0	0	0	0	0	0	0	0	0	0	0	0	0	0	0	0	0	0	0	0	0	0	0	0	0	0	0	0	0	0	0	0	0	0	0
90°S	1	0	0	0	0	0	0	0	0	0	0	0	0	0	0	0	0	0	0	0	0	0	0	0	0	0	0	0	0	0	0	0	0	0	0	0	0

The release grid is based on electrical power use (1 = 6×10^6 kW) from World Energy Supplies Table 25 [*United Nations*, 1978]. The indices *I*, *J* refer to the CTM with an 8° × 10° grid. See Table C2*b* for specific releases according to gas.

*United States and Canada.

†Western Europe, Australia, South Africa, and Japan. Japan has been scaled down by a factor of 2 because of its higher electricity/CFC ratios.

‡Rest of world.

TABLE C2b. CFC Weightings for Geographic Release Grid

Gas	Year	Weighting Factors
CFC-11	1970–1975	10[*] + 10[†] + 1[‡]
CFC-11	1976–1982	6[*] + 10[†] + 2[‡]
CFC-12	1970–1975	10[*] + 10[†] + 2[‡]
CFC-12	1976–1982	6[*] + 10[†] + 5[‡]

*United States and Canada.
†Western Europe, Australia, South Africa, and Japan. Japan has been scaled down by a factor of 2 because of its higher electricity/CFC ratios.

ed for initialization, and a summary of the individual experiments.

C1. *Release Scenarios*

Releases of CFCs to the atmosphere occur during primary manufacture, product application, and final disposition [see *McCarthy et al.*, 1977; *Gamlen et al.*, 1986]. There are no known natural sources: total production provides thus an upper limit to emissions. Estimates for the industrial production of CFC-11 and CFC-12 have been given by the *Chemical Manufacturers Association* (*CMA*), [1982, 1983, 1984, 1985]. Totals for Western reporting companies are believed to be accurate to better than 2%. Values for Soviet and Eastern European production for the period 1968–1975 are extrapolated from data given by Ye. P. Borisenkov and Yu. Ye. Kazakov (Effects of freons and halocarbons on the ozone layer of the atmosphere and climate, unpublished Russian manuscript, 1977; hereafter called Borisenkov and Kazakov, 1977). Large uncertainty is associated with the estimates of Soviet and Eastern European production. This has small effect on the CFC-11 budget, since these countries are minor sources of the gas. Production of CFC-12 in the U.S.S.R. and Eastern Europe could be quite important, especially if the growth rates reported for 1968–1975 (17% per year) persisted to later years. Original CMA reports included assumptions on the growth of emissions from the U.S.S.R. and Eastern Europe. More recent reports [*CMA*, 1984, 1985] specifically avoided estimates for Soviet production. The problem of deriving CFC-12 sources has led to considerable discussion and to revision of recent estimates for global emission [*Rowland et al.*, 1982; *Cunnold et al.*, 1983*b*; *Cunnold*, 1984].

We adopted the CMA estimates for production of CFCs between 1940–1982, as indicated in Table C1. Data on the seasonality of CFC release are lacking, and therefore the release was assumed to occur uniformly throughout the year. Our test of the global model focuses on its ability to reproduce observed spatial and seasonal patterns. If there was significant seasonal variation in emissions, we would expect observed concentrations to exhibit a noticeable annual cycle [see *Hyson et al.*, 1980].

Consumption patterns for CFC products in individual countries are not well established, and the spatial distribution for emissions cannot be defined with precision. Major CFC applications, such as use in aerosol propellants (52% of European market in 1983 [*CEFIC*, 1985]) rigid and flexible foams (20% and 11%, respectively) and refrigeration (12%), are associated with technologically advanced economies. We therefore used electric power consumption as a surrogate to construct a release pattern for CFCs. Electric power use reflects both national wealth and technology, and data are readily available for most countries. An 8° × 10° emission grid (1 unit = 6×10^6 kW) was defined, as illustrated in Table C2, and the world was subdivided into three economic groupings, each with its own coefficient relating CFC use to electrical power. The groupings selected were (1) the United States (U.S.A.) and Canada, (2) Western Europe, Japan, Australia, and South Africa, and (3) the rest of the world (ROW).

The weighting factor relating CFC emissions to consumption of electricity for each group is given in Table C2 for 1974 and for 1979. There was a shift in use of CFCs from North America to Western Europe between 1974 and 1979, and the ROW became an increasingly important factor especially for CFC-12. Release rates from 1970 through 1975 were computed using the 1974 factors, which correspond to the time of maximum growth in fluorocarbon use immediately prior to the oil crisis and the U.S. ban on CFCs in aerosol propellants. Release rates from 1976 through 1982 employed weighting factors for 1979. Extension of the model to 1985 would require that the emission factors be reevaluated to reflect expanded use of CFC-11 and CFC-12 by the ROW. Table C3 summarizes the fragmentary information available for CFC production and use in various geographic regions for comparison with the scenarios adopted here. Note that recent reports from the Soviet Union [*U.S.S.R.*, 1986] claim a much higher production of CFC-11 than used here. The quantity of CFCs released in the southern hemisphere is estimated to be between 4% and 8% of the total. Uncertainty in this number does not significantly affect model results (e.g., the north-south gradient of CFCs), provided that the southern hemispheric CFCs account for less than 10% of the total emissions.

Emission of CFCs into the atmosphere is simulated in the CTM as a surface source. An amount equal to the emission (in kilograms per second) in a given grid square (P) over the time step (Δt) is added to layer 1, and the vertical slope is reduced accordingly to allow for the fact that the CFCs are added to the bottom of the layer,

$$\begin{aligned} S^1(t + \Delta t) &= S^1(t) + P\Delta t \\ S_z{}^1(t + \Delta t) &= S_z{}^1(t) - P\Delta t \end{aligned} \tag{C1}$$

Subsequent upward transport (and vertical homogenization of layer 1) is provided by dry convection, moist convection, and large-scale convergence. When sources are resolved within a grid square by their second-order horizontal moments (i.e., P_x, P_{xx}, P_y, P_{yy}, P_{xy}), the corresponding moments of the tracer distribution in layer 1 are augmented as per (C1). In order to avoid negative sources, limits are placed on the source moments in the same manner as on the tracer moments in the work by *Prather* [1986].

C2. *Stratospheric Chemical Loss*

Loss of a trace gas due to photochemical reactions in the stratosphere is an important component of the global budget of many species, particularly CFC-11 and 12. Destruction of CFCs may be represented as a first-order loss process (per second) with coefficient L. The value of L depends on local pressure, overburden of ozone, and solar angle. The rapid falloff with altitude of CFC mixing ratios reflects the increasing importance of chemical loss at high altitude. The scale height of CFC-11, for example, is about 2 km at an altitude of 25 km, less above.

It is difficult therefore to determine the profile of CFCs with any precision using the limited stratospheric resolution of the

current GCM (see Figure A1). Issues of stratosphere-troposphere exchange and the vertical distribution of CFCs in the stratosphere would require a model with greater vertical resolution above 150 mbar, one that is tuned for stratospheric studies as in the work by *Golombek and Prinn* [1986]. We are currently developing a 21-layer CTM which should address these questions.

For present purposes, though, we are concerned not with the details of the CFC distribution in the stratosphere, but rather with their abundance in the troposphere. This is set mainly by the geographic distribution of the source and by effects of tropospheric circulation. The removal mechanism in the stratosphere regulates the trend in global abundance over long time scales and can be treated adequately for present purposes as follows.

Observations of CFCs [*World Meteorological Organization (WMO)* 1982, 1986] show that the falloff in concentration generally occurs above 50 mb. Stratospheric loss of CFCs in the CTM is limited to the top two layers and is represented by the coefficients L_8 and L_9 (per second). These quantities were calculated from a one-dimensional photochemical model [see *Logan et al.*, 1978, 1981; *Prather et al.*, 1984] using climatological mean data for atmospheric structure and O_3 [*Cole and Kantor*, 1978; *Hilsenrath et al.*, 1979; *London and Angell*, 1982; *Hering and Borden*, 1964, 1967]. The vertical distribution of CFCs in the one-dimensional model is calculated in a self-consistent manner, with vertical diffusion limiting the supply of trace gas to the region of rapid destruction in the upper atmosphere. Bulk loss frequencies reflect the weighted integrals of the local loss $L(z)$, the atmospheric number density $N(z)$, and the tracer mixing ratio $f(z)$:

$$L_8 = \frac{\int_{150\ \text{mbar}}^{70\ \text{mbar}} L(z)f(z)N(z)\,dz}{\int_{150\ \text{mbar}}^{70\ \text{mbar}} f(z)N(z)\,dz} \tag{C2}$$

$$L_9 = \frac{\int_{70\ \text{mbar}}^{0.1\ \text{mbar}} L(z)f(z)N(z)\,dz}{\int_{70\ \text{mbar}}^{0.1\ \text{mbar}} f(z)N(z)\,dz} \tag{C3}$$

TABLE C3. Data on Geographical Production and Release of CFCs

Gas	Period	Category	Region	Percent of World Total*		
				Table 4	Reference	Source
CFC-11	1931–1984	sales	SH	5%	4%	*CMA* [1985]
CFC-12				6	5	
CFC-11	1974–1975	production	USSR	3	2	Borisenkov and
CFC-12				6	7	Kazakov (1977)
CFC-11	1974	production	U.S.A. and Canada	51	46	*OECD* [1980]
& 12		and use	W. Europe	32	35	
			Japan	6	5	
			Australia	2	2	
CFC-11	1979	production	U.S.A. and Canada	35	29	
& 12		and use	W. Europe	37	39	
			Japan	7	6	
			Australia	2	2	
CFC-11	1976–1980	use	Australia	2.1	1.8	*Australian Environment*
& 12						*Council* [1983]
CFC-11	1983	sales	EEC	46	48	*CEFIC* (1985)
			ROW	4	9	
CFC-12			EEC	41	29	
			ROW	9	13	
CFC-11	1980	release	SH	5.5	5.4	*Cunnold et al.*
CFC-12				5.7	7.0	[1983*a*, *b*]
CFC-11	1980	release	U.S.A. and Canada	38	44	*Golombek and*
			W. Europe	41	30	*Prinn* [1986]
			Far East	9	9	
			Australia	2	2	
			SH	6	7	
CFC-12	1980	release	U.S.A. and Canada	32	44	
			W. Europe	37	31	
			Far East	10	8	
			Australia	2	2	
			SH	6	8	
CFC-11	1984–1986	production	USSR	3	17	*U.S.S.R.* [1986]
CFC-12				6	7	

*The referenced values (percent of world total) are compared with the fractional emissions used here, derived from the geographical release pattern in Table C2. SH stands for all of southern hemisphere; EEC stands for W. Europe, Australia, New Zealand, and South Africa; ROW equals rest of world, excluding EEC, U.S.A., Canada, Mexico, Japan, U.S.S.R., Eastern Europe, and China [*CEFIC*, 1985]. OECD is Organization for Economic Cooperation and Development, Paris, France.

Thus the rate of loss in layer 9 of the CTM included also stratospheric loss above 10 mbar. Evaluation of L from the one-dimensional model is independent of the absolute scale of the mixing ratio. Most of the loss in layer 9 occurs near the top, and this effect is approximated by using the computed loss

$$S^9(t + \Delta t) = S^9(t) - L_9 S^9(t)\Delta t \quad \text{(C4)}$$

and reducing the vertical slope accordingly:

$$S_z{}^9(t + \Delta t) = S_z{}^9(t) - L_9 S^9(t)\Delta t \quad \text{(C5)}$$

In some of the first numerical experiments with CFCs the vertical slope in the stratosphere (layer 9) was reset each time step to that value expected from the high-resolution one-dimensional model which approximated the observations. This technique provided a more accurate subgrid parameterization of the distribution and loss of CFCs in the stratosphere, but it had the unwanted wide effect of introducing a numerical artifact at the lower boundry of layer 9, thereby enhancing CFC concentrations in layer 8 by a few percent, and it was dropped from the CTM.

Values for the loss frequency (L_8, L_9) are calculated as a function of season and latitude at 15° intervals, using the one-dimensional model, with results summarized in Table C4. The quantities at northern latitudes are used in southern latitudes at equivalent seasons. Losses are scaled according to the earth-sun distance, increasing by 3.3% in January and decreasing appropriately in July. A two-dimensional cubic spline is fitted through the latitude-by-season points as nodes. The CTM then evaluates L at the center of each 4° latitude zone on a monthly basis. The quantities are assumed to be zonally invariant. Losses are calculated and applied once every major time step, 4 hours of the 4° × 5° model. The simple method outlined here should mimic stratospheric loss without introducing artifacts into the simulation of the troposphere.

TABLE C4. Stratospheric Parameters for CFC-11 and CFC-12

Month	Latitude					
	0°N	15°N	30°N	45°N	60°N	75°N
CFC-11 Average Loss Frequency (0–70 mbar)						
January	0.569	0.347	0.172	0.259	0.108	(.00)
April	0.630	0.529	0.328	0.344	0.185	0.100
July	0.521	0.551	0.504	0.389	0.335	0.222
October	0.649	0.563	0.358	0.220	0.160	0.077
CFC-11 Average Loss Frequency (70–150 mbar)						
January	0.065	0.026	0.003	0.000	0.000	(.00)
April	0.082	0.062	0.021	0.004	0.000	0.000
July	0.058	0.068	0.059	0.028	0.009	0.002
October	0.085	0.067	0.030	0.006	0.001	0.000
CFC-12 Average Loss Frequency (0–70 mbar)						
January	0.121	0.088	0.068	0.117	0.055	(.00)
April	0.129	0.114	0.101	0.140	0.093	0.059
July	0.114	0.118	0.112	0.117	0.128	0.104
October	0.132	0.120	0.088	0.081	0.077	0.045
CFC-12 Average Loss Frequency (70–150 mbar)						
January	0.006	0.002	0.000	0.000	0.000	(.00)
April	0.007	0.006	0.002	0.000	0.000	0.000
July	0.005	0.006	0.005	0.003	0.001	0.000
October	0.008	0.006	0.003	0.001	0.000	0.000

Units are yr^{-1}.

C3. *Initialization of Numerical Experiments*

A CFC simulation was initiated at a model time of January 1, 1970, with the following conditions. The total global abundance of CFC-11 and 12 was taken from the time-depenent integration of release given in Table C1. The hemispheres were longitudinally and latitudinally well mixed. Mixing ratios in stratospheric layers 8 and 9 were reduced by factors of 0.84 and 0.32 relative to tropospheric values for CFC-11. These factors were derived from observed stratospheric profiles [*WMO*, 1982, 1986]. Corresponding scale factors for CFC-12 were 0.91 and 0.53. The distribution adopted for January 1970 assumed a ratio of 1.20 for concentrations of CFC-11 in the northern hemisphere relative to those in the southern hemisphere [*Lovelock et al.*, 1974], with a value of 1.15 for CFC-12. Data for CFC-12 are not available for the early years, and the smaller value selected for the interhemispheric ratio is an estimate which reflects greater use of this compound more recently by developing countries at low latitudes. Results for CFC model runs are insensitive, after 1976, to details of the initialization procedure. The comparison with observations in this paper emphasizes the period of the published ALE data, 1978–1981.

A pilot calculation was performed involving a 12-year model run, simulating conditions from January 1, 1970, to January 1, 1982. A particular issue concerns the procedure for treatment of horizontal diffusion on subgrid scales. In a first series of runs, covering the period 1970–1980, we used a globally uniform value of 8×10^5 m^2 s^{-1} for the horizontal diffusion coefficient. This value provided an acceptable simulation of the ALE data for CFC-11 from 1979–1980. Results from this preliminary run were used to examine the role of diffusion and to initialize the three-dimensional tracer fields for more intensive study subsequent to January 1, 1976.

The standard simulation of CFCs reported in this paper is based on a 6-year calculation for CFC-11 and 12, from January 1, 1976, to January 1, 1982. The reference model uses the 8° × 10° CTM and a diffusion length of $D = 250$ km. The CFC-11 simulation was repeated using the second year of winds from the 4° × 5° GCM and the 5-day convection patterns. Similarly, a parallel run was made for CFC-12 with $D = 177$ km. Calculation of one model year for one tracer requires 1 hour of CPU time on an Amdahl-V6. Summaries of the last 2 years from these simulations are given in Table 1 and are discussed in the main text.

Acknowledgments. We would like to thank R. Prinn of MIT for helpful discussions regarding the ALE data, and are indebted to D. Cunnold and F. Alyea for making the observations available. We have received significant assistance from our colleagues during the course of this research: J. Hansen, R. Ruedy, J. Lerner, and N. Habra at Goddard Institute for Space Studies and R. Yevich, C. Spivakovsky, J. Logan, D. Jacob and C. DeMore at Harvard. This research was supported by NASA's Earth Science and Applications Division, grants to Harvard University from NASA (NAGW-359, NAG5-719, NAG5-785) and grants from the National Science Foundation (ATM-81-17009, ATM-84-131153, ATM-86-06057).

REFERENCES

Arakawa, A., Design of the UCLA General Circulation Model, *Tech. Rep. 7*, 116 pp., Dep. of Meteorol., Univ. of Calif., Los Angeles, 1972.

Australian Environment Council, Environment, health and economic implications of the use of chlorofluorocarbons as aerosol propellants and possible substitutes, report, Aust. Environment Counc. and Natl. Health and Med. Res. Counc., Canberra, Australia, 1983.

Brice, K. A., R. G. Derwent, A. E. J. Eggleton, and S. A. Penkett, Measurements of CCl_3F and CCl_4 at Harwell over the period January 1975–June 1981 and the atmospheric lifetime of CCl_3F, *Atmos. Environ.*, *16*, 2543–2554, 1982.

Bullister, J. L., and R. F. Weiss, Anthropogenic chlorofluorocarbons in the Greenland and Norwegian seas, *Science*, *221*, 265–267, 1983.

Central Intelligence Agency, *The World Factbook*, Washington, D. C., 1984.

Charney, J. G., Fjortoft, R., and von Neumann, J., Numerical integration of the barotropic vorticity equation, *Tellus*, *2*, 237–254, 1950.

Chatfield, R. B., and P. J. Crutzen, Sulfur dioxide in remote ocean air: Cloud transports of reactive precursors, *J. Geophys. Res.*, *89*, 7111–7132, 1984.

Chemical Manufacturers Association, World production and release of CFC 11 and 12 through 1981, Report of the Fluorocarbon Program Panel, edited by J. C. Van Horn, Washington, D. C., 1982.

Chemical Manufacturers Association, Production, sales and calculated release of CFC 11 and 12 through 1982, Report of the Fluorocarbon Panel, edited by E. F. Gormley, Washington, D. C., 1983.

Chemical Manufacturers Association, Production and release data of CFC 11 and 12 based on reported data through 1983, Report of the Fluorocarbon Panel, edited by E. F. Gormley, Washington, D. C., 1984.

Chemical Manufacturers Association, Production, sales and calculated release of CFC 11 and 12 through 1984, Report of the Fluorocarbon Panel, edited by E. F. Gormley, Washington, D. C., 1985.

Cole, A. E., and A. J. Kantor, Air Force Reference Atmospheres, *AFGL-TR-78-0051*, Air Force Geophys. Lab., Bedford, Mass., 1978.

Covey, C., S. L. Thompson, and S. H. Schneider, "Nuclear winter": A diagnosis of atmospheric general circulation model simulations, *J. Geophys. Res.*, *90*, 5615–5628, 1985.

Cunnold, D. M., Fluorocarbon lifetimes and releases from 5 years of ALE data, paper presented at CSIRO Baseline Conference, Commonwealth Sci. and Ind. Res. Organ., Aspendale, Australia, Nov., 1984.

Cunnold, D. M., R. G. Prinn, R. A. Rasmussen, P. G. Simmonds, F. N. Alyea, A. J. Crawford, P. J. Fraser, and R. D. Rosen, The Atmospheric Lifetime Experiment, 3, Lifetime methodology and application to 3 years of $CFCl_3$ data, *J. Geophys. Res.*, *88*, 8379–8400, 1983*a*.

Cunnold, D. M., R. G. Prinn, R. A. Rasmussen, P. G. Simmonds, F. N. Alyea, C. A. Cardelino, and A. J. Crawford, The Atmospheric Lifetime Experiment, 4, Results for CF_2Cl_2 based on 3 years of data, *J. Geophys. Res.*, *88*, 8401–8414, 1983*b*.

Cunnold, D. M., R. G. Prinn, R. A. Rasmussen, P. G. Simmonds, F. N. Alyea, C. A. Cardelino, A. J. Crawford, P. J. Fraser and R. D. Rosen, Atmospheric lifetime and annual release estimates for $CFCl_3$ and CF_2Cl_2 from 5 years of data, *J. Geophys. Res.*, *91*, 10,797–10,817, 1986

Dahlquist, G., and A. Bjorck, *Numerical Methods*, Prentice Hall, Englewood Cliffs, N. J., 1974.

European Council of Chemical Manufacturer's Federations, *Halocarbon Trend Study 1983–1995*, European Fluorocarbon Technical Committee, a CEFIC Sector Group, Brussels, 1985.

Fraser, P. J., P. Hyson, I. G. Enting, and G. I. Pearman, Global distribution and southern hemispheric trends of atmospheric CCl_3F, *Nature*, *302*, 692–695, 1983.

Fraser, P. J., N. Derek, R. O'Brien, R. Shepherd, R. A. Rasmussen, A. J. Crawford, and L. P Steele, 3.3 Intercomparison of halocarbon and nitrous oxide measurements, 1976–1984, in *Baseline Atmospheric Program (Australia) 1983–1984*, edited by R. J. Francey and B. W. Forgan, Division of Atmospheric Research, Commonwealth Scientific and Industrial Research Organization, Melbourne, Australia, 1985.

Fung, I., K. Prentice, E. Matthews, J. Lerner, and G. Russell, Three-dimensional tracer model study of atmospheric CO_2: Response to seasonal exchanges with the terrrestrial biosphere, *J. Geophys. Res.*, *88*, 1281–1294, 1983.

Gamlen, P. H., B. C. Lane, P. M. Midgley, and J. J. Steed, The production and release to the atmosphere of $CFCl_3$ and CCl_2F_2, *Atmos. Environ.*, *19*, 1077–1085, 1986.

Gammon, R. H., J. Cline, and D. Wisegarver, Chlorofluoromethanes in the northeast Pacific Ocean: Measured vertical distributions and application as transient tracers of upper ocean mixing, *J. Geophys. Res.*, *87*, 9441–9454, 1982.

Gidel, L. T., Cumulus cloud transport of transient tracers, *J. Geophys. Res.*, *88*, 6587–6599, 1983.

Golombeck, A., A global 3-D model of the circulation and chemistry of long-lived atmospheric species, Ph.D. dissertation, Mass. Inst. of Technol., Cambridge, 1982.

Golombeck, A., and R. G. Prinn, A global three-dimensional model of the circulation and chemistry of $CFCl_3$, CF_2Cl_2, CH_3CCl_3, CCl_4, and N_2O, *J. Geophys. Res.*, *91*, 3985–4001, 1986.

Hansen, J., G. Russell, D. Rind, P. Stone, A. Lacis, S. Lebedeff, R. Ruedy, and L. Travis, Efficient three-dimensional global models for climate studies: Models I and II, *Mon. Weather Rev.*, *111*, 609–662, 1983.

Heimann, M., C. D. Keeling and I. Fung, Simulating the atmospheric carbon dioxide distribution with a 3-D tracer model, in *The Changing Carbon Cycle: A Global Analysis*, edited by J. R. Trabalka and D. R. Reichle, Springer-Verlag, New York, 1986.

Hering, W. S., and T. R. Borden, Ozonesonde observations over North America, vol. 2, *Environ. Res. Pap. 38*, *AFCRL-64-30(II)*, Air Force Cambridge Res. Lab., Cambridge, Mass., 1964.

Hering, W. S., and T. R. Borden, Ozonesonde observations over North America, vol. 4, *Environ. Res. Pap, 279*, *AFCRL-64-30(IV)*, Air Force Cambridge Res. Lab., Cambridge, Mass., 1967.

Hilsenrath, E., D. F. Heath, and B. M. Schlesinger, Seasonal and interannual variations in total ozone revealed by the Nimbus 4 backscattered ultraviolet experiment, *J. Geophys. Res.*, *84*, 6969–6979, 1979.

Holton, J. R., *An Introduction to Dynamic Meteorology*, Academic Orlando, Fla., 1972.

Hyson, P., P. J. Fraser, and G. I. Pearman, A two-dimensional transport simulation model for trace atmospheric constituents, *J. Geophys. Res.*, *85*, 4443–4455, 1980.

Jackman, C. H., and P. D. Guthrie, Sensitivity of N_2O, $CFCl_3$ and CF_2Cl_2 two-dimensional distributions to O_2 absorption cross sections, *J. Geophys. Res.*, *90*, 3919–3923, 1985.

Jacob, D. J., M. J. Prather, S. C. Wofsy, and M. B. McElroy, Global distribution of ^{85}Kr in the troposphere, *J. Geophys. Res.*, this issue.

Khalil, M. A. K., and R. A. Rasmussen, Gaseous tracers of Arctic haze, *Environ. Sci. Technol.*, *17*, 157–164, 1983.

Khalil, M. A. K., and R. A. Rasmussen, Increasing trend of carbon monoxide in the earth's atmosphere, *Science*, *224*, 54–56, 1984.

Ko, M. K. W., and N. D. Sze, A 2-D model calculation of atmospheric lifetimes for N_2O, CFC-11 and CFC-12, *Nature*, *297*, 317–319, 1982.

Levy, H., II, J. D. Mahlman, and W. J. Moxim, Tropospheric N_2O variability, *J. Geophys. Res.*, *87*, 3061–3080, 1982.

Levy, H., II, J. D. Mahlman, W. J. Moxim, and S. C. Liu, Tropospheric ozone: The role of transport, *J. Geophys. Res.*, *90*, 3753–3772, 1985.

Logan, J. A., M. J. Prather, S. C. Wofsy, and M. B. McElroy, Atmospheric chemistry: Response to human influence, *Philos. Trans. R. Soc. London, Ser. A*, *290*, 187–234, 1978.

Logan, J. A., M. J. Prather, S. C. Wofsy, and M. B. McElroy, Tropospheric chemistry: A global perspective, *J. Geophys. Res.*, *86*, 7210–7254, 1981.

London, J., and J. K. Angell, The observed distribution of ozone and its variations, in *Stratospheric Ozone and Man*, vol. 1, edited by F. A. Bauer and R. B. Ward, pp. 7–42, CRC Press, Boca Raton, Fla., 1982.

Lovelock, J. E., Atmospheric fluorine compounds as indicators of air movements, *Nature*, *230*, 379, 1971.

Lovelock, J. E., R. J. Maggs, and R. J. Wade, Halogenated hydrocarbons in and over the Atlantic, *Nature*, *241*, 194–196, 1974.

Mahlman, J. D, and W. J. Moxim, Tracer simulation using a global general circulation model: Results from a mid-latitude instantaneous source experiment, *J. Atmos. Sci.*, *35*, 1340–1378, 1978.

Mahlman, J. D., H. Levy, II, and W. J. Moxim, Three-dimensional tracer structure and behavior as simulated in two ozone precursor experiments, *J. Atmos. Sci.*, *37*, 655–685, 1980.

Malone, R. C., L. H. Auer, G. A. Glatzmaier, M. C. Wood, and O. B. Toon, Nuclear winter: Three-dimensional simulations including interactive transport, scavenging, and solar heating of smoke, *J. Geophys. Res.*, *91*, 1039–1053, 1986.

McAvaney, B. J., W. Bourke, and K. Puri, A global spectral model for simulation of the general circulation, *J. Atmos. Sci.*, *35*, 1557–1583, 1978.

McCarthy, R. L., F. A. Bower, and J. P. Jesson, The Fluorocarbon-

Ozone theory I, World production and release of CFC-11 and CFC-12 through 1975, *Atmos. Environ.*, *11*, 491–497, 1977.

National Oceanic and Atmospheric Administration, Geophysical Monitoring for Climatic Change, Summary Report 1984, *Rep. 13*, edited by E. C. Nickerson, Air Resour. Lab, Boulder, Colo., 1986.

Newell, R., G. Boer, and J. Kidsen, An estimate of the interhemispheric transfer of CO from tropical general circulation data, *Tellus*, *26*, 103–107, 1974.

Organization for Economic Cooperation and Development, *Statistics of Foreign Trade Annual*, Paris, France, 1980.

Owens, A. J., J. M. Steed, C. Miller, D. L. Filkin, and J. P. Jesson, The atmospheric lifetimes of CFC 11 and CFC 12, *Geophys. Res. Lett.*, *9*, 700–703, 1982.

Pack, D. H., J. E. Lovelock, G. Cotton, and C. Curthoys, Halocarbon behavior from a long time series, *Atmos. Environ.*, *11*, 329–344, 1977.

Penkett, S. A., K. A. Brice, R. G. Derwent, and A. E. J. Eggleton, Measurement of CCl_3F and CCl_4 at Harwell over the period January 1975–November 1977, *Atmos. Environ.*, *13*, 1011–1019, 1979.

Phillips, N. A., The general circulation of the atmosphere: A numerical experiment, *Q. J. R. Meteorol. Soc.*, *82*, 123–164, 1956.

Phillips, N. A., A coordinate surface having some special advantage for numerical forecasting, *J. Meteorol.*, *14*, 184–185, 1957.

Pinto, J. P., Y. L. Yung, D. Rind, G. L. Russell, J. A. Lerner, J. E. Hansen, and S. Hameed, A general circulation model study of atmospheric carbon monoxide, *J. Geophys. Res.*, *88*, 3691–3702, 1983.

Prather, M. J., Continental sources of halocarbons and nitrous oxide, *Nature*, *317*, 221–225, 1985.

Prather, M J., Numerical advection by conservation of second-order moments, *J. Geophys. Res.*, *91*, 6671–6681, 1986.

Prather, M. J., M. B. McElroy, and S, C. Wofsy, Reductions in ozone at high concentrations of stratospheric halogens, *Nature*, *312*, 227–231, 1984.

Prinn, R. G., P. G. Simmonds, R. A. Rasmussen, R. D. Rosen, F. N. Alyea, C. A. Cardelino, A. J. Crawford, D. M. Cunnold, P. J. Fraser, and J. E. Lovelock, The Atmospheric Lifetime Experiment, 1, Instrumentation and overview, *J. Geophys. Res.*, *88*, 8353–8367, 1983.

Rasmussen, R. A., M. A. K. Khalil, A. J. Crawford, and P. J. Fraser, Natural and anthropogenic trace gases in the southern hemisphere, *Geophys. Res. Lett.*, *9*, 704–707, 1982.

Rowland, F. S., S. C. Tyler, D. C. Montague, and Y. Makide, Dichlorodifluoromethane, CCl_2F_2, in the earth's atmosphere, *Geophys. Res. Lett.*, *9*, 481–484, 1982.

Russell, G. L., and J. A. Lerner, A new finite differencing scheme for the tracer transport equation, *J. Appl. Meteorol.*, *20*, 1483–1498, 1981.

United Nations, World energy supplies, table 25, Production, Trade and Consumption of Total Industrial and Public Electricity 1973–1978, Dep. of Econ. and Soc. Aff., Stat. Offic., New York, 1978.

U.S.S.R., Values reported by Soviets at Working Group VIII meeting, Natl. Oceanic and Atmos. Admin. Clim. Program, Leningrad, November 1986.

Warner, M. J., and R. F. Weiss, Solubilities of chlorofluorocarbons 11 and 12 in water and seawater, *Deep Sea Res.*, *32*, 1485–1497, 1985.

Weiss, W., A. Sittkus, H. Stockburger, and H. Sartorius, Large-scale atmospheric mixing derived from meridional profiles of krypton 85, *J. Geophys. Res.*, *88*, 8574–8578, 1983.

Wisegarver, D. P., and J. D. Cline, Solubility of trichlorofluoromethane (F-11) and dichlorodifluoromethane (F-12) in seawater and its relationship to surface concentrations in the North Pacific, *Deep Sea Res.*, *32*, 97–106, 1985.

World Meteorological Organization, The stratosphere 1981: Theory and measurements, *WMO Rep. 11*, Geneva, 1982.

World Meteorological Organization, Atmospheric ozone 1985: Assessment of our understanding of the processes controlling its present distribution and change, *WMO Rep. 16*, Geneva, 1986.

Zipser, E., The role of organized unsaturated convective downdrafts in the structure and rapid decay of an equatorial disturbance, *J. Appl. Meteorol.*, *8*, 799–814, 1969.

M. McElroy and S. Wofsy, Center for Earth and Planetary Physics, Harvard University, 29 Oxford Street, Cambridge, MA 02138.

M. Prather, D. Rind, and G. Russell, NASA Goddard Space Flight Center, Institute for Space Studies, 2880 Broadway, New York, NY 10025.

(Received September 4, 1986;
revised February 20, 1987;
accepted March 31, 1987.)